Title

Coupled Interfacial and Bulk Kinetics Govern the Timescales of Multiphase Ozonolysis Reactions

Journal

The Journal of Physical Chemistry A, 126(30)

ISSN

1089-5639

Authors

Willis, Megan D

Wilson, Kevin R

Publication Date

2022-08-04

DOI

10.1021/acs.jpca.2c03059

Peer reviewed

Coupled Interfacial and Bulk Kinetics Govern the Timescales of Multiphase Ozonolysis Reactions

Megan D. Willis[1] and Kevin R. Wilson[2]

[1]Department of Chemistry, Colorado State University, Fort Collins, CO, USA

[2]Chemical Sciences Division, Lawrence Berkeley National Lab, Berkeley, CA, USA

Abstract

Chemical transformations in aerosol impact the lifetime of particle-phase species, the fate of atmospheric pollutants, and both climate and health-relevant aerosol properties. Timescales for multiphase reactions of ozone in atmospheric aqueous phases are governed by coupled kinetic processes between the gas-phase, the particle interface and its bulk, which respond dynamically to reactive consumption of O_3. However, models of atmospheric aerosol reactivity often do not account for the coupled nature of multiphase processes. To examine these dynamics, we use new and prior experimental observations of aqueous droplet reaction kinetics, including three systems with a range of surface affinities and ozonolysis rate coefficients (*trans*-aconitic acid ($C_6H_6O_6$), maleic acid ($C_4H_4O_4$) and sodium nitrite ($NaNO_2$)). Using literature rate coefficients and thermodynamic properties, we constrain a simple two-compartment stochastic kinetic model, which resolves the interface from the particle bulk and represents O_3 partitioning, diffusion and reaction as a coupled kinetic system. Our kinetic model accurately predicts decay kinetics across all three systems, demonstrating that both the thermodynamic properties of O_3 and the coupled kinetic and diffusion processes are key to making accurate predictions. An enhanced concentration of adsorbed O_3, compared to gas and bulk phases, is rapidly maintained and remains constant even as O_3 is consumed by reaction. Multiphase systems dynamically seek to achieve equilibrium in response to reactive O_3 loss, but this is hampered at solute concentrations relevant to aqueous aerosol by the rate of O_3 arrival in the bulk by diffusion. As a result, bulk-phase O_3 becomes depleted from its Henry's Law solubility. This bulk-phase O_3 depletion limits reaction timescales for relatively slow-reacting organic solutes with low interfacial affinity (i.e., *trans*-aconitic and maleic acids, with $k_{rxn} \sim 10^3$ - 10^4 M^{-1} s^{-1}), which is in contrast to fast-reacting solutes with higher surface affinity (i.e., nitrite, with $k_{rxn} \sim 10^5$ M^{-1} s^{-1}) where surface reactions strongly impact observed decay kinetics.

Correspondence to megan.willis@colostate.edu and krwilson@lbl.gov

1. Introduction

Atmospheric aerosol properties have important implications for climate, air-quality and health.[1-3] Multiphase aerosol chemical transformations govern the fate of particle phase species, including organic pollutants,[4, 5] and both climate and health-relevant aerosol properties.[6-8] The rates and mechanisms of these reactions are governed not only by the concentrations of atmospheric oxidants (e.g., O_3, OH radicals), but also by the variable composition of organic and inorganic aerosol components and the often significant fraction of liquid water.[9-11] To understand these chemical transformations, we need to consider multiphase reaction dynamics in concentrated to dilute aqueous phases relevant to aqueous aerosol and cloud water, which may not reflect the purely organic aerosol systems that are often the focus of mechanistic laboratory studies.[12-15]

In tropospheric multiphase reactions, O_3 is an important oxidant that enters the condensed phase through partitioning from the gas phase. This Henry's Law partitioning into atmospheric aqueous phases is governed by two coupled adsorption-desorption and solvation-desolvation equilibria; connecting the gas, interface and bulk phases.[16, 17] The position of these two coupled equilibria will respond dynamically to the consumption of O_3 by both interfacial and bulk reactions, such that O_3 transport and chemical reaction are inherently coupled.[15] A large number of reaction rate coefficients from beaker-scale laboratory experiments are available for atmospherically relevant aqueous phase ozonolysis reactions.[18] However, to use these bulk rate coefficients to predict reaction timescales in atmospheric aqueous phases we must be able to accurately represent how adsorption, desorption, solvation, desolvation and diffusion processes control multiphase reaction rates.[19-21] Further, evidence from both molecular dynamics simulations and experimental studies suggests that, compared to gas and bulk phases, O_3 is enhanced at the air-water interface.[22-25] Models of multiphase reactions must adequately capture the steady-state position of these coupled equilibria to predict characteristic reaction timescales.

Most models used to interpret and predict timescales for multiphase aerosol chemistry rely upon resistor model formulations for limiting cases of reactivity and diffusivity. In these resistor models, kinetic steps that hinder uptake and reaction are represented in analogy to resistances in electric circuits.[16, 21, 26, 27] To arrive at analytical expressions for reaction timescales, resistor models apply simplifying assumptions related to steady-state conditions, mixing, and decoupled surface and bulk processes.[21, 27] The resulting set of idealized limiting cases yields significant insight into heterogeneous and multiphase chemistry, and has allowed identification of potential rate-limiting processes over a range of experimental conditions.[3, 19, 27-32] For multiphase ozonolysis reactions, commonly applied limiting cases include: (1)

bulk reaction limited by ozone diffusion (i.e., reaction occurs in a thin shell below the interface, quantified by the reacto-diffusive length $L_{RD} = (D_{O3}\tau_{O3})^{1/2}$ where τ_{O3} is the chemical lifetime of O_3 in the condensed phase); (2) bulk reactions not limited by ozone diffusion (i.e., a dilute or "phase-mixed" limit[16]); and (3) interface-dominated reactions.[16, 21, 27 31, 32] A resistor model limiting-case, or combination of limiting cases, is fit to experimental data to yield an uptake coefficient (i.e., γ, the fraction of gas collisions that lead to reaction in, or on, the particle). Experimental data is then interpreted in the context of the limiting processes required to adequately account for observations.[30] This resistor approach is not computationally cumbersome; however, limiting cases often cannot describe the full range of atmospherically relevant regimes in particle-phase reactant concentrations and diffusivity, and by necessity neglect the coupled nature of interfacial and bulk processes.[21, 27]

Efforts to overcome some of these challenges can be characterized by three broad approaches. First, the resistor model limiting cases can be extended to incorporate additional resistances to particle phase uptake.[21] For example, a resistor model conductance for diffusion of particle-phase reactants has been derived and improves the accuracy of resistor model fits for viscous particles where diffusion of both reactants becomes limiting.[21, 30] Second, flux-based kinetic multilayer models have been coupled with inverse modelling to infer kinetic parameters by fitting the model to large sets of experimental data.[28, 33-37] These depth-resolved models can address previous challenges in representing non-uniform mixing, and provide insight into the coupling between reaction and diffusion in viscous systems.[38-40] However, without extensive and targeted experimental data sets,[34] this approach can result in under-constrained models. Even for well-studied pure organic systems, such as oleic acid,[15] challenges arise in reconciling inverse-modelled kinetic parameters with experimental values. A third approach is to build kinetic models with computational and experimental constraints on elementary reaction steps. This approach aims to provide predictive, albeit simple, models that can be tested against experiment without adjustable parameters.[41, 42] While this approach is independent of the numerical modelling tools used, it has been coupled with stochastic kinetic simulations[43] to represent aerosol multiphase and heterogeneous chemistry in both pure organic and aqueous aerosol systems oxidized by OH or O_3.[42, 44-48] For O_3 oxidation of pure organic sub-micron aerosol (e.g., squalene,[13] tricosene[45]) such models have indicated that only near-surface O_3 reactions can explain the observed particle-phase decay timescales, whereas bulk reactions driven by Henry's Law O_3 partitioning provide kinetics that are too slow to explain experimental results.[13, 49] These particular model frameworks have not been challenged with aqueous aerosol systems and micron-sized

particles, where the coupled nature of O_3 partitioning kinetics, diffusion and reaction may become important.

Existing models of multiphase O_3 chemistry often do not account for coupling of interfacial partitioning kinetics with diffusion and reaction, which may be important for predicting the timescale of bimolecular reactions in atmospheric aqueous phases. In this work, we apply a physically-constrained stochastic kinetic model of multiphase O_3 chemistry to predict the timescales of reactions in levitated aqueous, micron-sized particles. We test our predictive model using three model systems with different reaction rate coefficients with O_3 and differing affinities for the interface (*trans*-aconitic acid ($C_6H_6O_6$), maleic acid ($C_4H_4O_4$) and sodium nitrite ($NaNO_2$)). Our predictive kinetic model illustrates how multiphase reactions are governed by coupled kinetic steps in the gas-phase, at the particle interface and in its bulk. Our aim is to provide a quantitative model framework for multiphase O_3 chemistry that can be extended to quantify rate-limiting processes over a wide range of reaction conditions where traditional resistor model limiting cases may not be applicable.

2. Methods

Table 1: Experimental conditions for the ozonolysis of aqueous *trans*-Aconitic Acid (AA) droplets.

Exp. No.	RH (%)	O_3 (ppm_v)	r_0 (Microns)	$[AA]_0$ (molec. cm^{-3})	$[AA]_0$ (M)
1	87.9 ± 0.6	58.4	9.23	1.9×10^{21}	3.2
2	88.1 ± 1.3	65.2	9.06	1.9×10^{21}	3.2
3	90.9 ± 0.6	79.9	10.18	1.63×10^{21}	2.7
4	89.6 ± 2.2	78.1	10.76	1.76×10^{21}	2.9
5	89.6 ± 1.3	79.4	9.11	1.76×10^{21}	2.9

In our experiments, we monitor loss of particle-phase *trans*-aconitic acid (AA) via O_3 reaction in a monodisperse population of micron-sized aqueous particles (RH > 85%, Table 1) in a linear quadrupole electrodynamic trap (QET), coupled to single-droplet mass spectrometry and optical single-droplet sizing. Below we describe the QET, single-droplet mass spectrometry techniques, and the experimental sequence for studying multiphase reaction kinetics in the QET.

2.1 Quadrupole Electrodynamic Trap. The branched quadrupole electrodynamic trap (QET) confines charged droplets along the axis of the quadrupole trapping electrodes, and is described in Willis *et al*.,[50] and Jacobs *et al*.[51] Aqueous micron-sized droplets are generated with a piezoelectric droplet

dispenser (Microfab, Inc., MJ-ABP-01, 30μm orifice), and are introduced into the QET branch and subjected to an induction voltage (± 100 – 500 V) to induce a net charge on the droplet. Charged droplets are confined in the electric field generated by four stainless steel trapping electrodes, with an AC amplitude of 100 – 500V and frequency of 100 – 500 Hz. Droplets fall in a humidity-controlled gas flow approximately 12 cm to the lower portion of the QET, where they are held by a static DC voltage (up to ± 500 V) applied to a balancing electrode.

The linear QET traps multiple droplets simultaneously, which facilitates time-resolved experiments with a monodisperse droplet population (variability in diameter on the order of ± 2.5%) with consistent chemical composition. Two balancing electrodes are fixed approximately 6 cm apart along the lower portion of the QET providing multiple compartments for droplet trapping. A population of tens to hundreds of droplets (depending on size and charge) is dispensed through the QET branch at constant droplet dispenser voltage and pulse width, and trapped in the upper compartment. A single droplet is then moved from the upper to the lower compartment by setting the upper DC balancing voltage to zero for a duration of 1 – 50 ms. The single droplet trapped in the lower compartment is then sized, as described below, and ejected from the trap into the ionization region of an atmospheric pressure mass spectrometer with the aid of a humidity-controlled gas flow (Fig. S1).

2.2 QET environmental control. The QET is enclosed in an environmentally controlled chamber at ambient temperature (297.5 ± 0.5 K), where humidity is controlled by a zero air flow of 500 cm^3 min^{-1} (STP), split into a dry flow and a wet flow that passes through a water bubbler. The portion of wet and dry flows are controlled by mass flow controllers (MKS instruments), and their relative magnitude determines the relative humidity in the trap, which was monitored with an RH probe (Honeywell International Inc., HIH-4602C, ± 3.5% accuracy) at the QET inlet. Experiments were performed at high humidity (Table 1). Ozone was generated by passing a small flow of oxygen, 20 – 100 cm^3 min^{-1} (STP), through a corona discharge ozone generator, and diluting the resulting flow with 2 – 4 L min^{-1} (STP) of nitrogen. The resulting flow (100 – 700 ppm_v O_3) was sampled by an ozone monitor (2B Technologies, model 202M) and a small portion, 35 – 70 cm^3 min^{-1} (STP), was diverted through a rotameter and mixed with the gas flow entering the QET.

2.3 Droplet sizing. Trapped droplets are illuminated axially with a 532 nm laser (ThorLabs, CPS532), introduced from the top of the QET and focused toward the lower sizing compartment. Scattered light is collected on two CCD cameras (ThorLabs, DCC1645C) for droplet sizing and vertical droplet positioning in the lower QET compartment.[51, 52] The scattering angle for droplet sizing (19.6°) was

measured using polystyrene latex spheres of known size (24.61 ± 0.22 μm diameter). Droplets are sized using interference fringes in the Mie scattering pattern collected at 90° to the incident light, with the method described by Davies.[53] Briefly, angular peak positions (maxima in the angular scattering pattern) are iteratively compared with a library of expected peak positions, generated with Mie theory over a range of size and refractive index. The droplet refractive index is estimated from calculated droplet composition and water content (described below) and allowed to vary over a range (1.45 ± 0.03). The mean squared error between reference and recorded peak positions is minimized to extract the best fit droplet size.[53] This method can provide radius measurements with an accuracy of up to ± 60 nm from micron-sized droplets.[53]

2.4 Single Droplet Ambient Ionization Mass Spectrometry. All measurements used a Q Exactive Orbitrap Mass Spectrometer (ThermoFisher Scientific). The instrument was operated in negative ion mode, with a typical scan range of m/z 50 – 200, a resolution of 17500 and a maximum inject-time of 50 ms, resulting in a scan rate of 8 – 9 Hz. The QET was positioned above the mass spectrometer inlet and was coupled to a home-built ambient pressure ionization source by a grounded, stainless steel exit tube. Two complementary ionization sources are used in these experiments: paper spray ionization[50, 54, 55] and thermal desorption coupled to helium glow discharge ionization.[50, 56] Development and use of these ion sources for detection of single micron-sized droplets is described in detail in Jacbos *et al.*,[51] Kohli & Davies [54, 55] and Willis *et al.*[50] Their operation is summarized below.

Measurements of ozonolysis kinetics of *trans*-aconitic acid were made by thermally desorbing single particles and ionizing the resulting gas with helium glow discharge (GD) ionization near the inlet of the Q Exactive Orbitrap (Fig. S1). A home-built helium GD ionization source was coupled to a temperature-controlled vaporization platform for single droplet detection. The GD source is similar to that described by Upton *et al.*,[56] and was constructed from 1/16" tungsten electrodes housed in a glass flow cell with a 0.5 L min^{-1} (STP) helium flow. The needle electrode operated at 3 kV with a current of ~2.7 mA limited by a 1MΩ (10 W) resistor, and a discharge gap of 2.5 mm from the ground electrode. This configuration corresponds to the corona-to-glow discharge (DART-like) regime described by Shelley *et al.*[57] Outflow from the GD source entered a heated stainless steel vaporizing block held at ground. The vaporizer temperature was controlled with a cartridge heater and a temperature controller (Omega Engineering, CN9300). Ejected droplets impact the heated substrate in the QET gas flow and the resulting gas phase molecules intersect with the GD outflow in the ionization region to form ions sampled by the MS. The total flow directed toward the MS inlet was 1.0 L min^{-1} (STP), with an absolute humidity a factor of two lower than that in the QET due to dilution by dry helium. Droplet size and composition, and

vaporization temperature, were manipulated such that no evidence for reagent ion depletion was observed during single droplet detection events.[50]

Paper spray (PS) ionization was used primarily for confirmation of product ions detected by GD ionization, and identification of additional fragile products not detectable by thermal desorption. Whatman grade SG81 silica-coated chromatography paper was cut into triangular substrates using a universal laser cutter to create triangular substrates with a base of 8 mm and height of 10mm, leading to a spray tip angle of ~45 degrees. PS substrates were mounted in a stainless steel alligator clip to apply a negative voltage of 3 – 5 kV. Solvent (80:20 v/v HPLC grade CH_3OH:$CHCl_3$) was continuously supplied to the underside of the substrate with a PEEK delivery tube connected to a syringe pump operating at 20 μL min^{-1}. The PS substrate was positioned below the QET outlet such that sharp single droplet events were observed with duration ~1 – 4 seconds. Single droplets with polarity opposite to that of the PS ion source likely impacted near the tip of the PS substrate.[50, 54, 55]

2.5 Data collection and analysis. After trapping a droplet population, initial sizing and MS detection of unreacted single droplets, the dry component of the QET flow is replaced by an equal mass flow containing ozone, such that the relative humidity in the QET is maintained. Trapped droplets are exposed to ozone for a period of time, during which the outflow of the QET is sent to exhaust, and the size of a single droplet is monitored in the sizing compartment. After an exposure time has elapsed, ozone introduction into the QET is switched off and a series of single droplets ($n > 8$) are individually sized and ejected for MS detection, so that ozone is not present in the ionization region during droplet detection. This approach avoids unwanted gas-phase ozone (i.e., ion-molecule) chemistry in the ionization region.[58] To improve the signal-to-noise ratio of product ions, multiple droplets ($n = 3 – 5$) can be ejected simultaneously from the lower QET compartment. By repeating the above process over the course of minutes to hours, we obtain kinetics of the reaction between droplet components and ozone (Fig. S1).

Raw mass spectra were analyzed using the python based pymsfilereader (available at: github.com/frallain/pymsfilereader, using python 3.7.3), and Thermo Xcalibur. Time series of relevant exact masses, or background-subtracted mass spectra corresponding to single or multiple droplets, were extracted for further analysis. A single droplet detection event was defined as a signal with magnitude > 5 standard deviations above a running mean baseline. Detected droplet signals were integrated to provide the peak area corresponding to a single droplet at a particular exact mass-to-charge ratio, and these integrated signals are averaged over several ($n > 8$) single droplets at each ozone exposure. Data analysis code is available at github.com/willismd.

3. Model Formulation

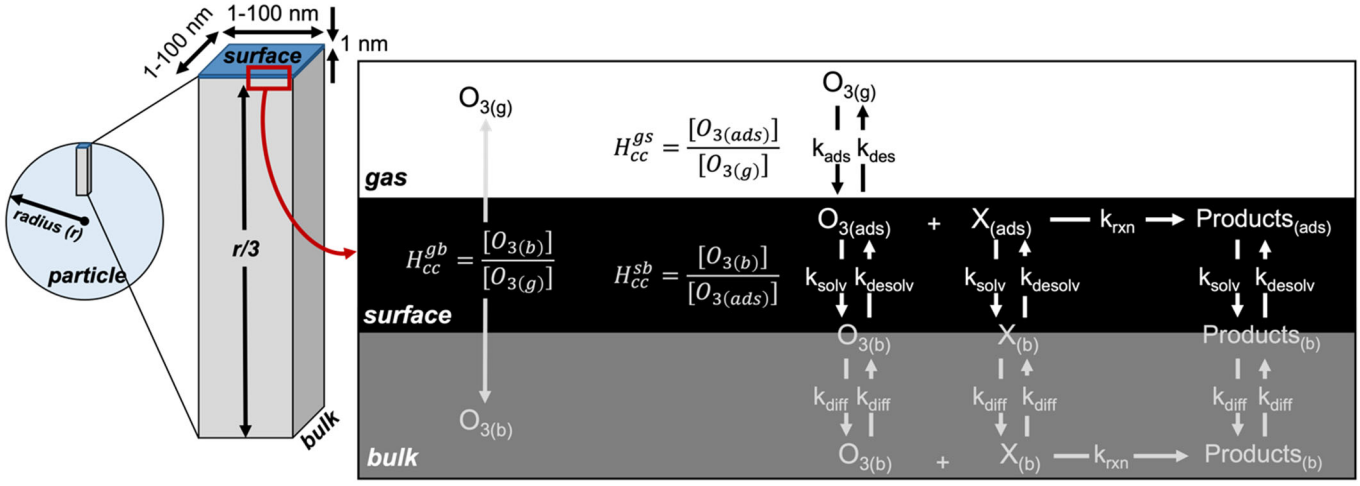

Figure 1. Overview of modelling approach and framework. **(Left)** Schematic showing the rectangular prism simulation geometry, which corresponds to the dimensions of a spherical particles with radius = r.[42, 47] The prism consists of a surface volume that is 1 nm thick (thickness chosen to be consistent with the estimated free energy profile for trace gas adsorption, see Section 3.3), which represents the interface and is located on top of a bulk compartment that has height of r/3. **(Right)** Overall modeling scheme that includes three coupled equilibria comprised of sets of forward and reverse kinetics steps that govern O_3 Henry's Law partitioning (i.e., adsorption (ads), desorption (des), solvation (solv), desolvation (desolv)). These kinetic steps are coupled with reactions of adsorbed species at the interface, and diffusion (diff) of solvated species into the bulk where they become available for bulk reaction.

3.1 Overall kinetic scheme. We represent the multiphase reaction of ozone using three coupled equilibria comprised of sets of forward and reverse kinetic steps, as well as both interfacial and bulk reactions (Fig. 1).[16, 17, 59-61] Our model does not assume equilibrium is reached, rather the kinetics of each forward and backward elementary step are represented explicitly. Organic molecules, both reactants and products, can diffuse and partition from the bulk to the interface. For example, the magnitude of surface partitioning of *trans*-Aconitic Acid (i.e., AA = X) at equilibrium ($AA_{(ads)} \leftrightarrow AA_{(bulk)}$) is described by rate coefficients for its solvation into the bulk and desolvation to the interface (k_{solv} and k_{desolv}). O_3 appears in gas and bulk-phases and at the interface. The interfacial and bulk concentrations are controlled by two coupled equilibria, whose product is the overall gas-bulk Henry's law coefficient,[17] H_{cc}^{gb}. The adsorbed O_3 concentration is governed by the gas phase ozone concentration [$O_{3(g)}$] and its adsorption (k_{ads}) and desorption (k_{des}) rate coefficients, while the bulk concentration is controlled by the rate coefficients for solvation (k_{solv}) and desolvation (k_{desolv}) of adsorbed O_3 and the diffusion coefficient (represented by the pseudo-first order rate coefficient for diffusion, k_{diff}, in Fig. 1). In Section 3.4 – 3.10, we describe the

elementary steps needed to represent the processes depicted in Fig. 1, and how we constrain the relevant rate coefficients from prior literature and Molecular Dynamics simulations.

3.2 Simulation Software. Kinetiscope©,[43] an open access software package, is used to numerically simulate the multiphase reaction of O_3 with *trans*-Aconitic Acid (AA). Kinetiscope© uses a stochastic algorithm to propagate the chemical evolution of a system by randomly selecting among probability-weighted elementary reaction and diffusion steps, and is well-suited to numerically solving stiff systems.[62, 63] Models built with this software package have been used extensively to predict heterogeneous and multiphase transformations in submicron aerosols,[13, 14, 41, 42, 44, 47, 64] as well as micron-sized emulsions that require quantitative descriptions of surface and bulk reactions, diffusion, and evaporation.[65]

Table 2: List of elementary reaction, partitioning and diffusion steps with rate coefficients for the surface and bulk compartments of the explicit kinetic simulations for *trans*-Aconitic Acid

	Elementary Step	Rate Coefficient				
No.	***Surface***	**Forward**	**units**	**Reverse**	**Units**	**Ref.**
S1	$O_{3(g)} + O_3\_Site \leftrightarrow O_{3(ads)}$	$(9.0 \times 10^{-11}) \cdot \sigma$	$cm^3\ molec.^{-1}\ s^{-1}$	5.4×10^{6}	s^{-1}	a,b,c,d
S2	$O_{3(ads)} \leftrightarrow O_{3(b)} + O_3\_Site$	4.6×10^{5}	s^{-1}	2.8×10^{-15}	$cm^3\ molec.^{-1}\ s^{-1}$	a,b,c,d
S3	$AA_{(ads)} + O_{3(ads)} \rightarrow C_4\_CI_{(ads)} + Glyoxylic\ Acid_{(ads)}$	1.4×10^{-17}	$cm^3\ molec.^{-1} s^{-1}$			e
S4	$C_4\_CI_{(ads)} \rightarrow C_3\_Product_{(ads)}$	7.9×10^{7}	s^{-1}			f
S5	$C_4\_CI_{(ads)} + Glyoxylic\ Acid_{(ads)} \rightarrow C_6\_SOZ_{(ads)}$	1.3×10^{-18}	$cm^3\ molec.^{-1} s^{-1}$			f
S6	$C_4\_CI_{(ads)} + O_{3(ads)} \rightarrow C_4\_Product_{(ads)}$	4.0×10^{-13}	$cm^3\ molec.^{-1} s^{-1}$			f
S7	$AA_{(b)} + Site \leftrightarrow AA_{(ads)}$	1.2×10^{-20}	$cm^3\ molec.^{-1} s^{-1}$	90	s^{-1}	g
S8	$C_4\_CI_{(b)} + Site \leftrightarrow C_4\_CI_{(ads)}$	5.1×10^{-20}	$cm^3\ molec.^{-1} s^{-1}$	90	s^{-1}	g
S9	$Glyoxylic\ Acid_{(b)} + Site \leftrightarrow Glyoxylic\ Acid_{(ads)}$	2.7×10^{-21}	$cm^3\ molec.^{-1} s^{-1}$	90	s^{-1}	g
S10	$C_3\_Product_{(b)} + Site \leftrightarrow C_3\_Product_{(ads)}$	1.2×10^{-20}	$cm^3\ molec.^{-1} s^{-1}$	90	s^{-1}	g
S11	$C_4\_Product_{(b)} + Site \leftrightarrow C_4\_Product_{(ads)}$	5.1×10^{-20}	$cm^3\ molec.^{-1} s^{-1}$	90	s^{-1}	g
S12	$C_6\_SOZ_{(b)} + Site \leftrightarrow C_6\_SOZ_{(ads)}$	1.2×10^{-20}	$cm^3\ molec.^{-1} s^{-1}$	90	s^{-1}	g
S13	$Glyoxylic\ Acid_{(ads)} \rightarrow Glyoxylic\ Acid_{(g)} + Site$	1.0×10^{5}	s^{-1}			h
	Diffusion Pathways	**Diffusion Coefficient**				
D1	$AA_{(b)}$ (Bulk) $\leftrightarrow AA_{(b)}$ (Surface)	8.4×10^{-6}	$cm^2\ s^{-1}$			i
D2	$C_4\_CI_{(b)}$ (Bulk) $\leftrightarrow C_4\_CI_{(b)}$ (Surface)	8.3×10^{-6}	$cm^2\ s^{-1}$			i
D3	$Glyoxylic\ Acid_{(b)}$ (Bulk) $\leftrightarrow Glyoxylic\ Acid_{(b)}$ (Surface)	1.2×10^{-5}	$cm^2\ s^{-1}$			i
D4	$C_3\_Product_{(b)}$ (Bulk) $\leftrightarrow C_3\_Product_{(b)}$ (Surface)	1.1×10^{-5}	$cm^2\ s^{-1}$			i
D5	$C_4\_Product_{(b)}$ (Bulk) $\leftrightarrow C_4\_Product_{(b)}$ (Surface)	8.9×10^{-6}	$cm^2\ s^{-1}$			i
D6	$C_6\_SOZ_{(b)}$ (Bulk) $\leftrightarrow C_6\_SOZ_{(b)}$ (Surface)	7.2×10^{-6}	$cm^2\ s^{-1}$			i
D7	$O_{3(b)}$ (Bulk) $\leftrightarrow O_{3(b)}$ (Surface)	1.76×10^{-5}	$cm^2\ s^{-1}$			j
	Bulk	**Rate Coefficient**				
B1	$AA_{(b)} + O_{3(b)} \rightarrow C_4\_CI_{(b)} + Glyoxylic\ Acid_{(b)}$	1.4×10^{-17}	$cm^3\ molec.^{-1} s^{-1}$			e
B2	$C_4\_CI_{(b)} \rightarrow C_3\_Product_{(b)}$	7.9×10^{7}	s^{-1}			f
B3	$C_4\_CI_{(b)} + Glyoxylic\ Acid_{(b)} \rightarrow C_6\_SOZ_{(b)}$	1.3×10^{-18}	$cm^3\ molec.^{-1} s^{-1}$			f
B4	$C_4\_CI_{(b)} + O_{3(b)} \rightarrow C_4\_Product_{(b)}$	4.0×10^{-13}	$cm^3\ molec.^{-1} s^{-1}$			f

a: Vacha *et al.*[22]; **b**: Vieceli *et al.*[23]; **c**: Sander[66]; **d**: Utter *et al.*[67], Hu *et al.*[68], Magi *et al.*[69], Schütze *et al.*[70], Müller & Heal[71]; **e**: Leitzke & von Sonntag, **f**: Vereecken *et al.*[72]; **g**: Bleys and Joos[73]; **h**: Wiegel *et al.*[42]; **i**: Bidstrup and Geankoplis[74]; **j**: Gottschalk *et al.*[75]; σ is the sticking coefficient.

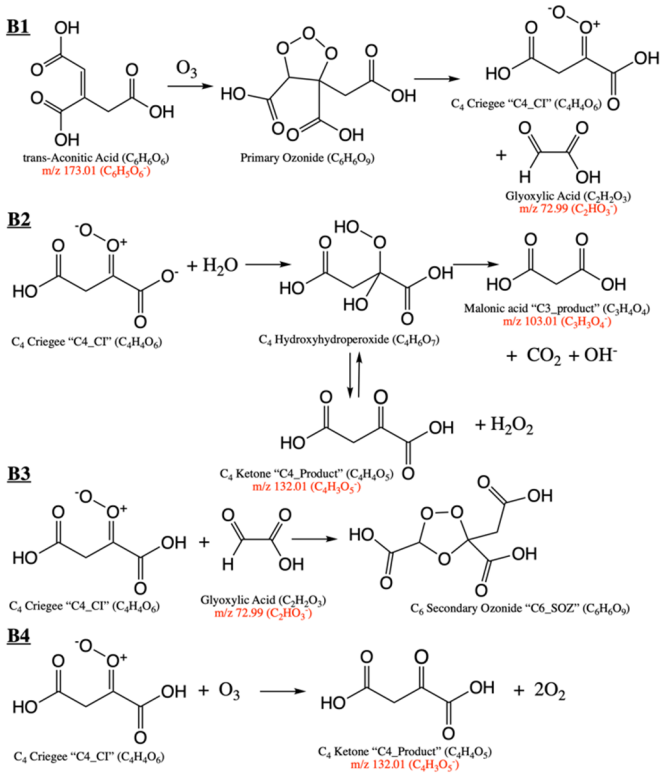

Figure 2. Reaction scheme for ozonolysis of *trans*-Aconitic Acid, showing reaction pathways and molecular structures of reactants and potential products. Products identified by single-droplet mass spectrometry are noted in red, with their measured exact masses and negative ion molecular formulas. A dominance of ≥C_3 products, and glyoxylic acid, (Fig. S3 & S4) in reacted particles suggests that the primary ozonide decomposes preferentially to form the C_4 Criegee Intermediate (B1). We note that the expected C_4 ketone product (B2) was observed at very low signal intensities in all experiments despite its structural similarity to other products detected with high relative signal intensity (e.g., Malonic acid, "C3_Product"), suggesting other possible important reaction pathways (B2). While fragmentation of both the highly oxygenated *trans*-Aconitic Acid and its reaction products complicates spectral interpretation, we see no evidence that the fate of the C_4 Criegee intermediate impacts the loss rate of *trans*-Aconitic Acid under these high humidity conditions.

3.3 Simulation Geometry. To model a spherical droplet with radius = r, Houle and coworkers[42, 47] showed that a rectangular prism simulation geometry, with a height of r/3, could be used (Fig. 1). Here, the prism is divided into two sub-volumes: a surface, and a bulk region below. Molecules move between these volumes by Fickian diffusion. This simulation geometry preserves the correct scaling between interface and bulk processes and is computationally more efficient than simulating an entire sphere. We assume that each sub-volume is instantaneously mixed. This assumption was tested with additional simulations where the single bulk volume, shown in Fig. 1, was divided up into smaller sub-volumes. For these test simulations the concentrations of reactants and products were uniform and we did not observe the formation of concentration gradients in $[AA_{(b)}]$. Concentration gradients do form in $[O_{3(b)}]$ since under aqueous aerosol conditions the reacto-diffusive length for ozone (on the order of 200 – 300 nm for AA

under our experimental conditions) is less than the particle radius for micron-sized aerosol. However, our model aims to represent kinetically distinct regions (i.e., interface, or surface volume, and bulk), and does not resolve bulk-phase gradients in [$O_{3(b)}$].

The length and width of the prism are 1 X 1 nm (Fig. 1). The simulation results presented below are insensitive to these dimensions and were checked by using larger 100 nm x 100 nm x r/3 nm simulation volumes (Fig. S2). These expanded dimensions correspond to a 4 order of magnitude change in the total number of molecules in the simulation. An additional parameter is required to define the surface volume (i.e. the interface thickness, δ). A thickness of 1 nm is used and is selected to be reasonably consistent with the width of the solvation free energy profile observed for trace gas adsorption in Molecular Dynamics simulations.[22-25] Surface thickness is used to convert surface concentrations (i.e., molecules cm^{-2}) to surface volume concentrations (i.e., molecules cm^{-3}).

3.4 Bulk Reaction Steps. We use a series of elementary reaction and diffusion steps in the explicit simulation (Table 2), with four elementary reaction steps in the bulk compartment (Fig. 2). Step B1 describes the reaction of dissolved $O_{3(b)}$ with AA. To our knowledge, the rate coefficient for the ozonolysis of AA has not been measured so instead we use a rate constant for a suitable proxy (i.e. fumaric acid, $C_4H_4O_4$) measured in the bulk aqueous phase by Leitzke and von Sonntag.[76] Fumaric acid and AA both have a *trans* structure around the C=C moiety. We expect that the decomposition of the primary ozonide (Fig. 2) is very fast and therefore we do not include this unimolecular step explicitly. The products of step B1 are a Criegee intermediate (CI) and a carbonyl. From the carbon number distribution of the products (Fig. S3 & S4), as well as previous experiments,[13] we infer that the POZ decomposes asymmetrically to form mainly a C_4 –CI (Fig. 2) on a secondary carbon atom, and glyoxylic acid (see B1, Fig. 2). Once formed, the CI can react with water (B2) or the carbonyl co-product (B3), likely within the same solvent cage. In the aqueous phase, the rate coefficient for B2 is assumed to be 4.3 x 10^{-15} cm^3 $molec.^{-1}$ s^{-1}; a value computed[77] for a gas phase CI with the water dimer ($(H_2O)_2$). Step B2 is expressed as a pseudo first order rate coefficient using the [H_2O] in the droplet (see below and Table 2). Mass spectra of reacted droplets (Fig. S3 & S4) using both glow-discharge and paper spray ionization show a predominance of $>C_2$ products, as well as glyoxylic acid, which we expect to efficiently evaporate from the particles during the reaction time. The apparent importance of C_3 product ions may be consistent with decarboxylation of the C_4 hydroxy hydroperoxide (shown in Fig. 2 and by Leitzke and von Sonntag[76]); however, if this mechanism is a two-electron process, as suggested by Leitzke and von Sonntag[76], it would require a deprotonated acid group to proceed, which appears unlikely under our experimental conditions (see

Section 3.5). These C_3 product ions may also arise from decarboxylation during particle detection with either ionization method (Fig. S3), so we do not interpret the implications of our observed product ion distributions further. The rate coefficient for step B3, is taken from a prior heterogeneous ozonolysis study,[13] in which this rate constant was constrained as part of a larger kinetic model. The rate constant for CI + O_3 (B4) is from Vereecken *et al.*[77] and is based on coupled cluster calculations in combination with theoretical kinetic predictions. We do not include reaction of the CI with carboxylic acids in this aqueous system, because available experimental evidence suggests that this pathway is not observed in the presence of large water concentations.[78, 79] Thus, our assumptions about the fate of the CI do not alter the overall decay rate of AA, which is the main focus of this study.

We assume that these elementary steps (B1-B4) also occur at the interface (S3-S6) albeit with reactants in their adsorbed states (i.e. $AA_{(ads)}$ + $O_{3(ads)}$); consistent with a Langmuir Hinshelwood mechanism. In the absence of any knowledge about the magnitude of the interfacial rate coefficients for these reactions we assume that they proceed in the surface volume with the same rate coefficients as used in the bulk.

3.5 Bulk Concentrations and Density. The AA concentration and water content in the particles were estimated using the Aerosol Inorganic-Organic Mixtures Functional groups Activity Coefficients (AIOMFAC) model (aiomfac.lab.mcgill.ca)[80] and the experimental relative humidity (Table 1, Fig. S5). Aconitic acid is described in AIOMFAC using a functional group contribution method, which assumes that organic acid functionalities remain protonated. This assumption is reasonable for our experimental conditions as predictions of particle pH from the Extended AIM Aerosol Thermodynamics Model (E-AIM, aim.env.uea.ac.uk)[81, 82] indicate a pH < 2, and the first pKa of *trans*-Aconitic Acid is 2.91, [83] so we do not expect that the carboxylic acid groups are significantly deprotonated. For the organic systems studied here, we neglect ionic strength effects on the O_3 Henry's Law constant (see Section 3.9) and on the ozone-organic reaction rate coefficients.

Densities for each of the species in the simulation are shown in Table S1. These molar volumes in addition to vapor pressures (described below) are required to accurately predict the change in droplet size during the reaction. We do not account for changes in hygroscopcity that might accompany the formation of the ozonolysis products, which would alter the water content and therefore the size of the droplet.

3.6 Diffusion Pathways. Reactants, products and intermediates enter and exit the bulk-phase by solvation from (k_{solv}), and desolvation to (k_{desolv}; Fig. 1), the interface. Once solvated, these species are allowed to move within the bulk compartment by gradient diffusion according to Fick's Law, such that a rate of

diffusion is calculated as $\pm D[X_{bulk}]A$ (where D is the diffusion coefficient in $cm^2\ s^{-1}$, $[X_{bulk}]$ is the bulk concentration of any diffusing species, and A is the compartment area) . Once molecules diffuse into the surface compartment, they can either adsorb (S7-S12) or diffuse back into the bulk. Diffusion constants of all of the organic species are estimated using the semi-empirical relationship developed by Bidstrup and Geankoplis[74] for aqueous molecular diffusivities of carboxylic acids. The diffusion constant of O_3 in water is fixed to a literature value of $D = 1.76 \times 10^{-5}\ cm^2\ s^{-1}$.[75] For the experimental relative humidity range explored here (Table 1), the AIOMFAC model (aiomfac.lab.mcgill.ca) estimates dynamic viscosities, for the organic – water mixture, to be 1.12×10^{-2} – 8.03×10^{-3} Pa s, which is in the range where diffusion coefficients for ozone in aqueous organic particles approach that in pure water.[39]

3.7 Interfacial Reaction Steps. In addition to the reaction steps S3-S6 listed in Table 2, we define a series of steps that describe the adsorption and desorption kinetics of molecules to/from the interface as shown conceptually in Fig. 1. Using a Langmuir[84] framework, this is implemented in the simulation by defining the concentration of available adsorption sites (i.e., "Sites" in S7-S13) in the surface compartment.[44] For the organic molecules in the simulation we assume that a site corresponds to a mean molecular area of 66 $Å^2$. This corresponds to a maximum interfacial concentration (Γ_∞) of 1.5×10^{14} molecules cm^{-2} and is consistent with a series of C_7 to C_9 di-carboxylic acids.[73] Interfacial concentration is converted to a volumetric concentration using the interface thickness, δ, which we set to 1 nm to be consistent with the width of the free energy profile for trace gas adsorption (Section 3.3). The depth of the interface in our simulations is significantly smaller than the reacto-diffusive length of O_3 (> 200 nm). During the simulation, adsorption sites are conserved, and we assume that all organic species compete for the same set of adsorption sites. For the adsorption and desorption of O_3, a separate set of sites is defined (termed "O_3_site" in S1 and S2), corresponding to the smaller molecular area of ozone of 18.5 $Å^2$, as computed by Vieceli et al.[23] If the interface were to become saturated the volumetric concentration of O_3 in the surface compartment would be 5.4×10^{21} molecules cm^{-3}.

We estimate adsorption and desorption rate constants using data reported by Bleys and Joos[73] for a series of water soluble compounds (e.g. alcohols and di-carboxylic acids). The desorption rate coefficients vary little with molecular structure or functional group and therefore we use a median value of 90 s^{-1} for all species in the simulation.[73] Adsorption rate coefficients strongly depend upon functional group (i.e. –OH vs. –COOH) and increase[73] exponentially with increasing carbon number. Extrapolating an exponential fit to the linear dicarboxylic acid data (Fig. S6) reported in Bleys and Joos[73] allows us to estimate the adsorption rate coefficient of the C_2, C_3, and C_4 product species in the simulation (S8-S11).

AA has three –COOH groups and thus we expect its adsorption rate coefficient is over-estimated relative to a dicarboxylic acid with the same carbon number. Instead, we estimate its adsorption rate coefficient based upon the surface tension data of citric acid; a structurally similar tri-acid. Citric acid is moderately surface active and depresses surface tension, as a function of mole fraction, to a similar extent as malonic acid ($C_3H_4O_4$).[85] Therefore, we use the C_3 adsorption rate coefficient as an estimate for AA and the C_6 SOZ, which also contains three –COOH groups. All of these organic species are highly water soluble and only moderately surface active, as can be shown using computed Langmuir isotherms with the adsorption/desorption rate coefficients shown in Table 2.

3.8 Evaporation. The C_2 carbonyl reaction product (glyoxylic acid) is the only product allowed to evaporate in the simulation. This is reasonable given the low volatility of the reactants (Fig. S7) and other major reaction products. The evaporation rate constant for glyoxylic acid in the simulation is computed, as described by Wiegel et al.,[42] using an estimated vapor pressure of 25 Pa from EPI Suite (US EPA Estimation Program Interface Suite, v 4.11).

3.9 Ozone Gas – Interface – Bulk Partitioning. Two equilibria govern the partitioning of ozone. First, the equilibria shown in step S1 (Table 2 and Fig. 1) describes the adsorption and desorption of gas phase ozone ($O_{3(g)}$) to and from the interface. Second, the equilibria shown in step S2, in turn, describes the kinetics of bulk solvation of adsorbed O_3 ($O_{3(ads)}$) and the reverse step of desolvation of bulk ozone ($O_{3(b)}$) to the interface. The product of the two corresponding equilibrium constants is the Henry's law constant for O_3 in H_2O, which from prior literature is H_{cp} = 1.11 (± 0.11) x 10^{-2} M atm^{-1} (H_{cc}^{gb} =0.27 ± 0.03, where H_{cp} is the Henry's Law constant defined by aqueous concentration and gas partial pressure, and H_{cc} is the unitless Henry's Law constant).[17, 66] H_{cc} < 1 indicates that O_3 is hydrophobic relative to other atmospheric oxidants[22] (e.g., OH, HO_2) and that the difference in solvation free energy of $O_{3(b)}$ relative to $O_{3(g)}$ is positive (i.e., $\Delta G_{sol(gb)}$ = +0.76 kcal mol^{-1}) computed from,[22]

$$H_{cc}^{gb} = exp\left(\frac{-\Delta G_{sol(gb)}}{RT}\right) \quad \text{Eq. (1)}$$

Molecular Dynamics (MD) simulations indicate that the change in solvation free energy of $O_{3(ads)}$ relative to $O_{3(g)}$ ($\Delta G_{sol(gs)}$) is negative. Together with $\Delta G_{sol(gb)} > 0$, this indicates that ozone is enriched at the interface compared to both the gas and bulk phases. The range of interfacial solvation free energies from prior MD simulations are: -1.2 kcal mol^{-1},[22, 24] -1.46 kcal mol^{-1},[23] -1.30 kcal mol^{-1}, [23] and -1.5 kcal mol^{-1} .[25] The variability in these energies is likely due to differences in computational methods; nevertheless, this range of free energies correspond to values of the gas-surface partitioning coefficient (H_{cc}^{gs}) of 7.6 - 12.5 (Eq. (1)). We constrain our model using the value reported by Vieceli et al.[23] (-1.30

kcal mol^{-1}), which is near the mean of previously predicted values and yields H_{cc}^{gs}= 8.9. We acknowledge that while H_{cc}^{gb} is well constrained (to within ± 11%) from prior literature, the magnitude of calculated interfacial solvation free energies and thus H_{cc}^{gs} is less certain, with predicted values varying on the order of 30% from H_{cc}^{gs}= 8.9. This uncertainty is necessarily reflected in elementary kinetic parameters, as described by the relationships below, but are not large enough to change mechanistic interpretations.

Since the product of H_{cc}^{gs} and H_{cc}^{sb} must necessarily yield the correct H_{cc}^{gb} (0.27) as determined by experiment, this implies that the change in solvation free energy for $O_{3(ads)} \rightarrow O_{3(b)}$ is positive (+ 2.06 kcal mol^{-1}) with a value of H_{cc}^{sb} = 0.03. The resulting surface enrichment of ozone relative to gas and bulk phases is illustrated in Fig. S8 with a simulation showing the non-reactive uptake of ozone and its time dependent concentrations in the gas, interface and bulk phases.

H_{cc}^{gs} corresponds to the equilibria in step S1 (Table 1), which consists of a forward adsorption (*ads*) and reverse desorption (*des*) step. At steady state, O_3 adsorption and desorption rates are equal so that,

$$k_{ads} \cdot [O_{3(g)}] \cdot [O_3\_site] = k_{des} \cdot [O_{3(ads)}] \qquad \text{Eq. (2)}$$

where k_{ads} is proportional to the rate of $O_{3(g)}$ entry into the surface compartment,

$$k_{ads} \cdot \sigma \; = \frac{1}{4} \cdot A \cdot \bar{c} \cdot \sigma = 9.0 \times 10^{-11} \; \cdot \sigma \; (cm^3 \; molec.^{-1} \cdot \; s^{-1}) \, . \qquad \text{Eq. (3)}$$

A is the area (1 x 1 nm^2) of the surface compartment, $\bar{c}$ is the mean speed of O_3 (360 m/s at 294K) and σ is the sticking coefficient per O_3_site. For the systems considered here we assume that there is 1 site (e.g., C=C bond) per molecule. The surface concentration (Γ_∞) of O_3, as described above, corresponds to a volumetric concentration of adsorption sites at the interface such that,

$$[O_3\_site] = \frac{\Gamma_\infty}{\delta} = \; 5.42 \times 10^{21} \; sites \cdot cm^{-3} \qquad \text{Eq. (4)}$$

yielding the following expression for H_{cc}^{gs},

$$H_{cc}^{gs} = \frac{[O_{3(ads)}]}{[O_{3(g)}]} = \frac{k_{ads} \cdot \Gamma_\infty \cdot \sigma}{k_{des} \cdot \delta} = 8.9 \qquad \text{Eq. (5)}$$

A similar expression can be written for the equilibrium shown in step S2 and its relationship to the surface to bulk partitioning coefficient, H_{cc}^{sb}, which relates [$O_{3(ads)}$] and [$O_{3(b)}$]. At steady state,

$$k_{solv} \cdot \left[O_{3(ads)}\right] = k_{desolv} [O_{3(b)}] \cdot [O_3\_site] \qquad \text{Eq. (6)}$$

which yields the following expression,

$$H_{cc}^{sb} = \frac{[O_{3(b)}]}{[O_{3(ads)}]} = \frac{k_{solv} \cdot \delta}{k_{desolv} \cdot \Gamma_\infty} = 0.03 \qquad \text{Eq. (7)}$$

The relationships shown in Eqs. (5) and (7) constrain the ratios of k_{solv} to k_{desolv} , k_{ads} to k_{des} and k_{solv} to k_{des}, which is summarized in Eq. (8a) and (8b).

$$H_{cc}^{gb} = H_{cc}^{gs} \cdot H_{cc}^{sb} = \frac{[O_{3(ads)}]}{[O_{3(g)}]} \cdot \frac{[O_{3(b)}]}{[O_{3(ads)}]} = \frac{k_{ads} \cdot \Gamma_\infty \cdot \sigma}{k_{des} \cdot \delta} \cdot \frac{k_{solv} \cdot \delta}{k_{desolv} \cdot \Gamma_\infty} = \frac{k_{ads} \cdot \sigma}{k_{des}} \cdot \frac{k_{solv}}{k_{desolv}} \quad \text{Eq. (8a)}$$

$$H_{cc}^{gb} = H_{cc}^{gs} \cdot H_{cc}^{sb} = 8.9 \times 0.03 = 0.27 \quad \text{Eq. (8b)}$$

Equation (8a) is analogous to previous formulations of the Henry's Law constant in terms of adsorption, desorption, solvation and desolvation rate coefficients, as presented by Hanson 1997 (their Eq. 8b),[60] Remorov and George, 2006 (their Eq. 18),[61] Pöschl *et al.,* 2007 (their Eq. 73)[86] and Ammann *et al.,* 2013 (their Eq. 21).[59]

3.10 Determination of absolute values for σ, k_{ads}, k_{des}, k_{solv} and k_{desolv}. The above relationships constrain only the ratio of rate constants. As discussed extensively by Shi et al.,[87] determining the absolute values of k_{ads}, k_{des}, k_{solv} *and* k_{desolv} can be difficult because they depend upon the model framework used to describe trace gas uptake. For instance, while both the critical cluster nucleation and Gibb's surface excess models account for the experimental observations of ethanol uptake, the absolute values for k_{des} and k_{solv} differ by some 5 orders of magnitude.[87] This difference arises because both models preserve only key ratios, for example k_{solv}/k_{des}, which are constrained by the experimentally determined mass accommodation coefficient (α).[60, 88] Nevertheless, the relationships shown in Eqs. (2-8) do provide some additional constraints.

k_{ads} and k_{des} are not independent quantities since rearranging Eq. (5) yields,

$$k_{des}(s^{-1}) = \frac{k_{ads} \cdot \Gamma_\infty \cdot \sigma}{H_{cc}^{gs} \cdot \delta} \quad \text{Eq. (9)}$$

Eq. (9) shows that k_{des} is inversely proportional to H_{cc}^{gs}, or the interfacial solvation free energy, which means that for a larger free energy change between gas and partial solvation at the interface, k_{des} would necessarily become smaller. Using the values of Γ_∞, δ, H_{cc}^{gs} and k_{ads} derived above yields,

$$k_{des} = 5.48 \cdot 10^{10} \cdot \sigma \ (s^{-1}) \quad \text{Eq. (10)}$$

Equations (9) and (10) show that k_{des} is directly proportional to σ, the assumed sticking probability. If all of the incoming gas phase O_3 molecules collide with the interface and stick (i.e., σ =1), k_{des} = $5.48 \cdot 10^{10}$ s^{-1}, corresponding to a desorption lifetime ($\tau_{des} = k_{des}^{-1}$) of 18.2 ps. This is consistent with the simulated mean residence time of O_3 on a water slab.[89] Alternatively, if only a small fraction of the colliding molecules stick to the interface, and $\sigma = 10^{-4}$, then τ_{des} = 182 ns. This change in τ_{des} with σ is consistent with our intuition that the fraction of molecules that appear to "stick" on the liquid interface depends upon

the observation time. If the observation window is short (~ps), then all of the molecules that have impinged upon the interface appear frozen, yielding a value of $\sigma = 1$. However, over much longer observation timescales the fraction of impinging molecules that remain at the interface decreases so that $\sigma < 1$. In MD simulations[89] the fraction of O_3 sticking trajectories drops precipitously with the duration of the simulation; from 87% at 3 ps to 0.8% at 90 ps, which is the maximum simulation time. Pairs of σ and τ_{des} that both satisfy Eq. (10) and accurately describe a given experiment may be situational, to reflect the nature of the reaction mechanism.[90] If the interfacial reaction proceeds via an Eley Rideal type mechanism, where a prompt reaction occurs upon a gas phase collision with a surface molecule, then the larger fraction of molecules with short surface residence times (~10's of ps, on the order of a molecular vibration) might play a controlling role in the observed kinetics. Alternatively, the much smaller fraction of molecules with comparably longer interfacial residence times (~100-200 ns) would be more important for a Langmuir Hinshelwood mechanism that proceeds through long-lived adsorbed states. In reality, desorption times and corresponding sticking coefficients are likely best represented by a distribution of values.

Here, we find that predicted reaction kinetics are invariant if three criteria are satisfied (Fig. S9): σ is $\geq 10^{-4}$, Eq. (9) is satisfied, and the ratio $\frac{k_{solv}}{k_{des}}$ is constrained (described below) to experimental measurements of α. Therefore, given these criteria, potentially significant uncertainties in σ do not alter our model output significantly. To optimize simulation time for the results shown below we use $\sigma = 10^{-4}$ and $k_{des} = 5.48 \times 10^6$ s^{-1} (i.e. $\tau = 182$ ns). While not observed in the multiphase systems examined here, very fast reactions may lead to important sensitivity of the reaction kinetics to σ and τ_{des}.

We constrain the absolute values of k_{solv} and k_{desolv} from k_{des}. The ratio of k_{solv} to k_{des} governs the fraction of adsorbed molecules ($O_{3(ads)}$) that ultimately become solvated ($O_{3(b)}$) within the bulk liquid. This ratio ($\frac{k_{solv}}{k_{des}}$) is traditionally interpreted as the mass accommodation coefficient (α).[21, 60, 88] From prior measurements, α for O_3 in aqueous solutions ranges from 10^{-3} to 1 [67-71] as summarized in Müller and Heal.[71] From MD simulations[23] the ratio of absorption (solvation) to desorption probabilities for O_3 at an aqueous surface is ~0.06, and is within the range of these prior measurements of α. In steps S1 and S2 (Table 2) we use $\frac{k_{solv}}{k_{des}} = 0.085$, which is in the mid-range of previous measurements and consistent with estimates provided by MD simulations. Better constraints on α in the future will improve confidence in the estimation of $k_{solv.}$ Finally, a value of k_{desolv} is computed in order to provide the correct H_{cc}^{sb} yielding an overall Henry's law constant that is consistent with prior measurements (i.e., H_{cc}^{gb} as shown in Eq. (1)).

In summary, the rate coefficients and diffusion constants used in the kinetic simulation are directly obtained either from prior literature or are computed using experimentally validated parameterizations. The absolute values of σ, k_{ads}, k_{des}, k_{solv} and k_{desolv} used in the model are derived self-consistently to produce the correct values H_{cc}^{gb}, H_{cc}^{gs}, H_{cc}^{sb} and α, which are quantities constrained by prior experiments or molecular simulations.

4. Results & Discussion

To evaluate the coupled kinetic processes that drive O_3 multiphase reaction timescales, we use both new and prior experimental observations of multiphase ozone reactions with aqueous organic inorganic particles. Our aim is to use a single kinetic framework to explain reaction timescales across three systems (*trans*-aconitic acid, maleic acid and sodium nitrite). We emphasize that our simple kinetic model uses the minimum possible number of kinetic parameters to represent elementary steps, and does not include fitted parameters. We compare our predictive model to experimental particle-phase decay kinetics and use the model to identify processes that govern observed reaction timescales.

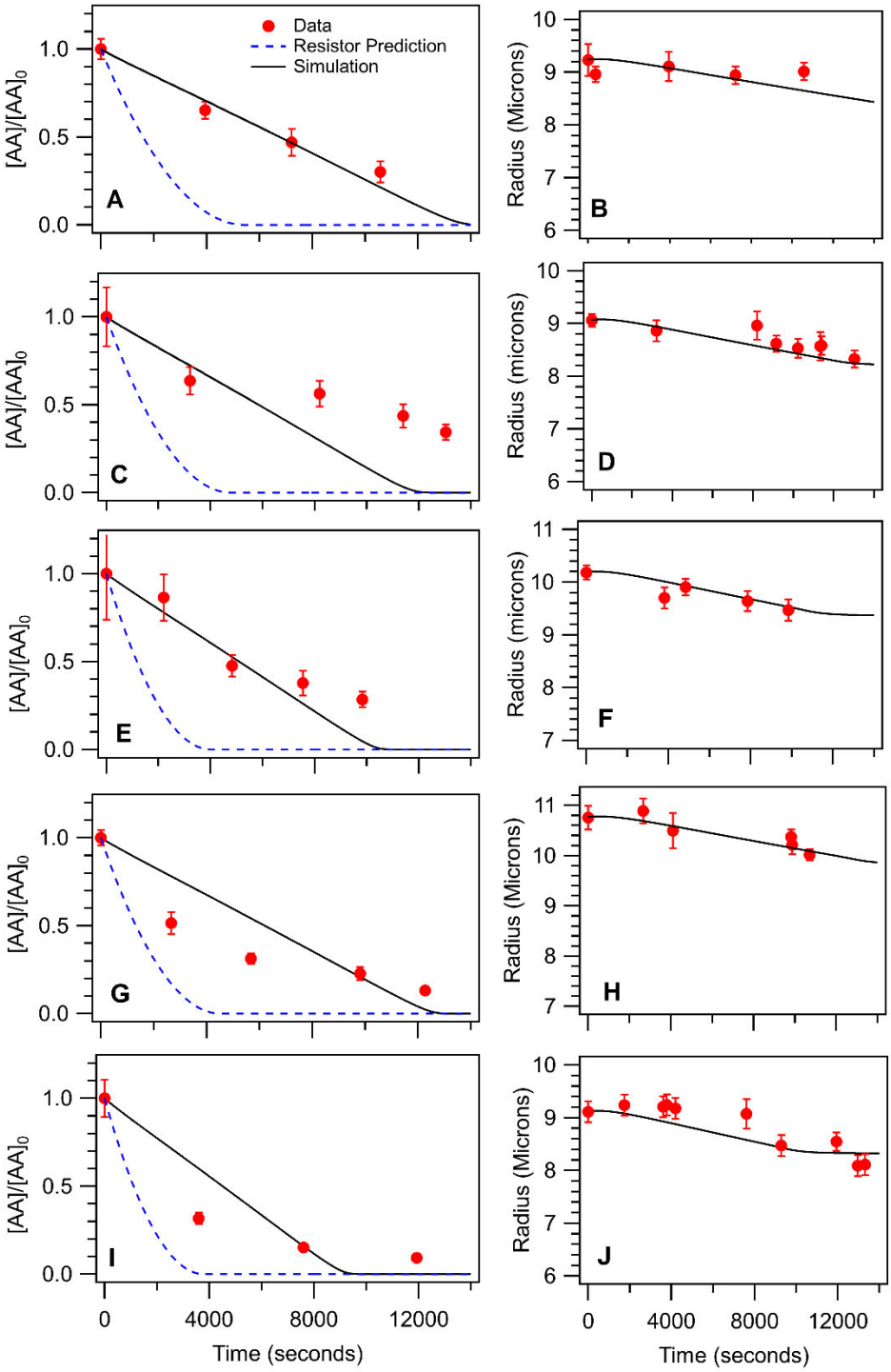

Figure 3. Decay of *trans*-Aconitic Acid (AA, left panels) and change in particle radius (right panels) vs. reaction time for experiments: #1 **(A,B)**, #2 **(C,D)**, #3 **(E,F)**, #4 **(G,H)**, #5 **(I,J)**. Table 1 shows the experimental conditions for experiments #1 – 5. Experimental data are shown as red circles (error bars for mass spectral and size data represent the standard deviation in measurements across multiple (n >8) single particles), explicit simulation predictions that include both interfacial and bulk reactions are solid black lines, and resistor model predictions (Eq. 11 & 12, using bulk rate coefficients, diffusion coefficients and Henry's Law constants identical to the explicit model) are shown in dashed blue lines.

4.1 Multiphase reaction of ozone with aqueous organic acids.

4.1.1 trans-Aconitic Acid (AA). Our simple two-compartment kinetic model, which represents kinetically distinct regions (interfacial volume and bulk), captures the particle size change and AA decay timescale across five sets of measurements (Fig. 3). Experimental model inputs are the measured $[O_{3(g)}]$, initial droplet radius (r_0) and $[AA]_0$ (Table 1). Each data point ($[AA]/[AA]_0$) in Fig. 3 corresponds to the mean peak area derived from multiple individual droplets ($n > 8$), which are sequentially sampled from a population of monodisperse droplets trapped together and simultaneously exposed to the same ozone concentration. Our explicit simulation predictions are consistent with the experimental reaction timescales (Fig. 3), though we do observe some variability in the experiments. This variability arises from differences in vaporization location and temperature, and ionization efficiency, as individual particles are ejected from the QET for analysis.[50] Our model's ability to predict experimental particle size validates our assumption that the major volatile product in this system is glyoxylic acid (see Sections 3.4 and 3.8), which is formed during the primary ozonide decomposition (Fig. 2) and is a co-product of the C_4 Criegee Intermediate.

Our simulations demonstrate that over the reaction time 92 – 88% of reactions between O_3 and AA occur in the particle bulk (Fig. S10). Despite the enriched concentration of adsorbed ozone at the interface, this occurs due to the relatively slow reaction of AA with O_3 and AA's low surface affinity (e.g., for Expt #1 in Table 1, $[AA_{(b)}] = 3.2$ M and from a Langmuir framework $[AA_{(ads)}] = 0.42$ M). The shape of the predicted decay kinetics from our explicit model (Fig. 3) are linear, which suggests that the multiphase reaction is zeroth-order in AA and is therefore governed by a process other than the bulk O_3 + AA reaction. Zeroth-order kinetics are also somewhat evident in the experimental data, but the number of data points, and their variability, in each experiment makes this conclusion difficult to draw from the experiment alone. In the predicted decay, the kinetics become more exponential in shape as $[AA_{(b)}]$ becomes more dilute near the end of the reaction time (Fig. 3). These observations provide evidence that O_3 transport into the particle bulk may limit the reaction rate in aqueous AA particles.

Since AA decay kinetics appear O_3 transport-limited, we might expect a resistor model that represents bulk reactions limited by O_3 diffusion[21] to accurately predict experimental reaction timescales. Previous studies support this expectation, as the reactive uptake coefficient (γ) in micron-sized aqueous droplets is frequently represented by this resistor limiting case.[27, 31, 71, 91, 92] AA is well-mixed within the particle on the timescale of reaction (i.e., assuming a Henry's Law concentration for O_3, the reacto-diffusive length, $L_{RD,AA} = (D_{AA}/k_{rxn}[O_3]_0)^{1/2}$, for AA is > 100 μm). However, in contrast to our simple two-

compartment model, which represents the average [$O_{3(b)}$], we do expect that a gradient in O_3 concentration forms within the particle bulk.[27] Therefore, the majority of bulk reactions occur in a layer with thickness on the order of the reacto-diffusive length for O_3 ($L_{RD,O3} = (D_{O3}/k_{rxn}[AA]_0)^{½}$, Section 3.3). With molar AA concentrations (Table 1) the reacto-diffusive length for ozone is smaller than the particle radius, and the decay of AA may be described by (i.e., in the limit where $L_{RD,O3} < r_0/20$):[21, 27]

$$\frac{[AA]}{[AA]_0} = \left(1 - \frac{3\cdot[O_{3(g)}]\cdot\gamma\cdot\bar{c}}{8\cdot r_0\cdot[AA]_0}\cdot t\right)^2 \qquad \text{Eq. (11)}$$

where,

$$\frac{1}{\gamma} = \frac{1}{\sigma} + \frac{1}{\alpha} + \frac{\bar{c}}{4H_{cp}\,RT\sqrt{Dk_{rxn}\cdot[AA]_0}} \qquad \text{Eq. (12)}$$

For example, for our Expt. #5 (Table 1) $L_{RD,O3}$ = 0.26 μm, which is less than $r_0/20$ = 0.46 μm. For a meaningful comparison, we use the same values in Eq. (12) for H_{cp} (1.11 x 10^{-2} M/atm), D_{O3} (1.76 x 10^{-5} cm^2 s^{-1}), σ (10^{-4}), α (8.5 x 10^{-2}), and k_{rxn} (1.4 x 10^{-17} cm^3 $molec.^{-1}$ s^{-1}) that were used in our explicit simulations. We note that Equations (11) and (12) neglect surface reactions, which appears a reasonable assumption in this system (Fig. S10). Using the experimental values for [$O_{3(g)}$], r_0 and $[AA]_0$ in Eqs. (11) and (12), we compare predicted kinetics from this resistor model limiting case with experimental data and explicit simulations (Fig. 3).

The predicted decay of AA using the resistor model is faster than our experimental observations and explicit stochastic simulations (Fig. 3). For example, using the reaction conditions from Expt. #1 in Eq. (12) yields γ = 1.7 x 10^{-5}. If we assume instead that σ = 1, the uptake coefficient is only marginally larger (2.0 x 10^{-5}) and the decay kinetics of AA are even faster. We note that under our experimental conditions, corrections to γ arising from gas phase diffusional resistance of O_3 are minor (< 0.1%).[19, 71] If instead, Eq. (11) is used to fit the data, by allowing γ to vary to best replicate the measurements, we obtain a value of $\gamma_{fit} \sim 4$ x 10^{-6} for experiment #1. This indicates that the explicit simulations, and our experimental observations, are a factor ~4 – 5 slower than the estimates provided by this resistor model limiting case.

In addition, resistor model predictions do not predict zeroth-order kinetics, but rather predict a more exponential-like decay of AA. We discuss the kinetic and diffusive steps that set the multiphase reaction timescale further in Sections 4.3.

Table 3. Maleic acid droplet ozonolysis experiments reported by Dennis-Smither *et al*. and shown in Fig. 5.

Droplet	RH (%)	O_3 (ppm)	R_0 (microns)	$[MA]_0$ (molec. cm^{-3})	$[MA]_0$ (M)
A	63	38 ± 8	4.59	4.46×10^{21}	7.4
B	72	38 ± 8	3.85	3.73×10^{21}	6.2
D	54	48 ± 10	4.58	4.94×10^{21}	8.2
E	64	52 ± 10	4.03	4.40×10^{21}	7.3
F	72	53 ± 10	4.72	3.85×10^{21}	6.4
H	62	65 ± 13	4.27	4.46×10^{21}	7.4

4.1.2 Maleic Acid (MA). We further test our explicit simulations using data for maleic acid ozonolysis reported by Dennis-Smither *et al*.[31] This data set (Table 3) is composed of ozonolysis studies in single micron-sized aqueous particles. The normalized decay kinetics of MA particles, obtained using Raman spectroscopy, and radius vs. reaction time are reproduced[31] in Fig. 4. We modified our explicit model of AA ozonolysis to account for differences in the rate coefficient for the O_3 + MA reaction, which is 6x slower[76] than for AA. Further, MA is more volatile than AA, and evaporates from the droplet over the course of the reaction (Fig. S7 & S11). In addition, the diffusion coefficients for MA and its reaction products were modified to account for differences in molecular size (Table S2). We compare our model results to a subset of data from Dennis-Smither *et al.*[31] recorded at RH < 73% (i.e., 6 individual droplet experiments, Table 3). We neglect the 3 experiments at RH > 73%, because particles grew during ozonolysis, likely due to an increase in hygroscopicity, which is a process not currently included in our model.

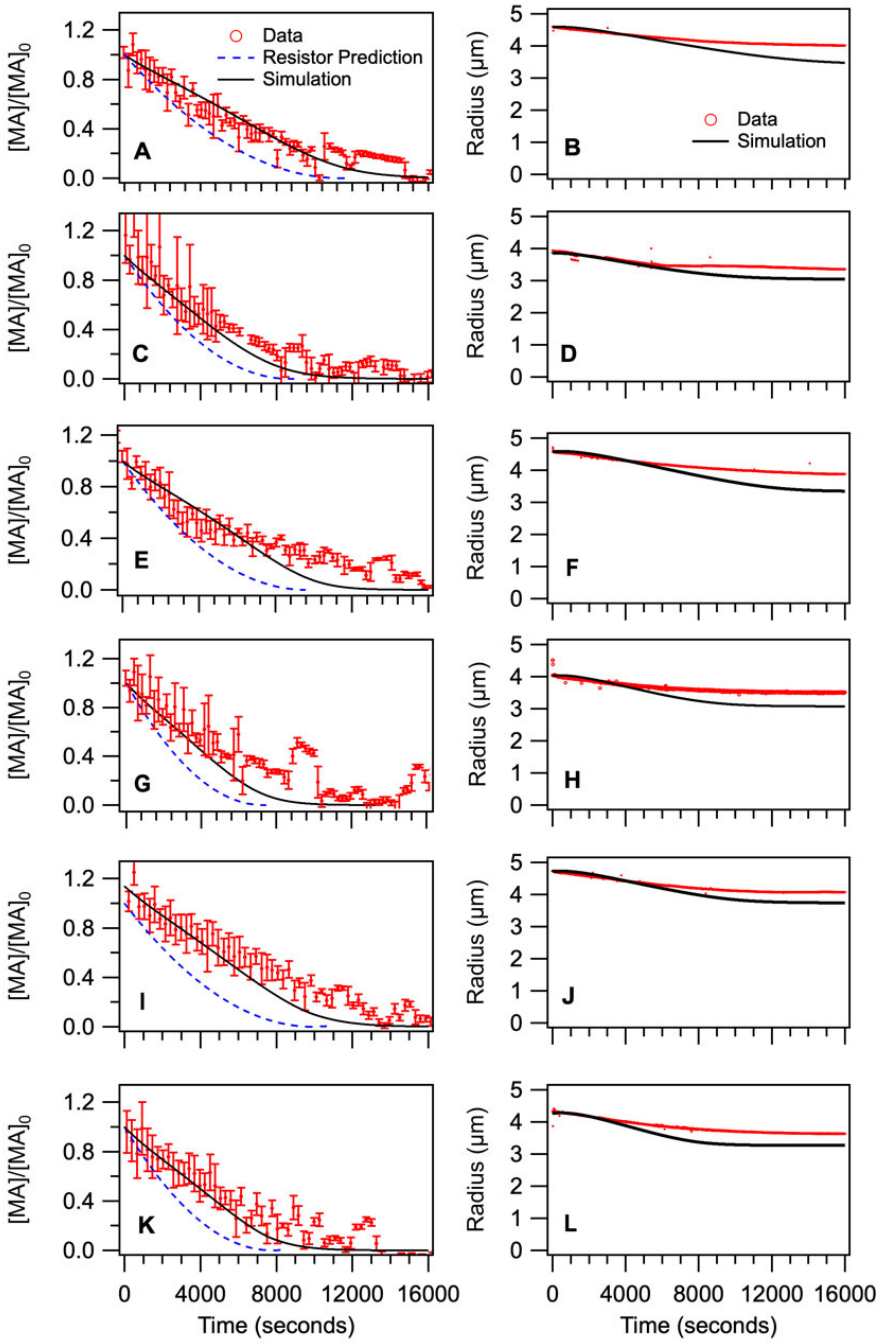

Figure 4. Maleic acid (MA) data reproduced from Dennis-Smither *et al.*[31] Decay of MA (left panels) and change in radius (right panels) vs. reaction time for particles: A **(A,B)**, B **(C,D)**, D **(E,F)**, E **(G,H)**, F **(I,J)** and H **(K, L)**. Table 3 shows the experimental conditions for particles A – H, reported by Dennis-Smither *et al.*[31] Solid black lines show explicit simulation predictions with both surface and bulk reactions, and dashed blue lines show resistor model predictions (Eq 11 & 12, using bulk rate coefficients, diffusion coefficients and Henry's Law constants identical to the explicit model).

Our explicit simulations can reasonably reproduce the decay kinetics of maleic acid as well as the decrease in droplet size with reaction time (Fig. 4). As is the case with AA, the predicted decay kinetics

appear nearly linear with reaction time, demonstrating kinetics that are zeroth-order in MA until near the end of the reaction. This feature is consistent with the MA experimental measurements, which have a higher time resolution than our AA dataset. The predicted decrease in droplet size at reaction times > 5000 seconds deviates from observations. The origin of this discrepancy could arise for two reasons. First, simulated changes in droplet size are sensitive to the assumed molecular density, in addition to volatility, of the reaction products relative to MA. Second, as noted above, the simulations do not account for any changes in hygroscopicity during the reaction, which was clearly evident in the Dennis-Smither *et al*[31] data recorded at RH > 73%. So, it is plausible for the reaction conditions shown in Table 3 there is a competition between chemical erosion (driven by volatility of glyoxylic acid) and hygroscopic growth that would account for the differences between the simulated particle size and observations.[92]

Similar to AA, our explicit simulations demonstrate that bulk reaction dominates the decay of MA. Over the reaction time, ~96% of reactions occur in the bulk, which is higher than for AA due largely to the smaller rate coefficient for reaction of MA with O_3 (Fig. S10). Despite the apparent validity of the common resistor model assumption that maleic acid ozonolysis in micron-sized particles should occur primarily in the bulk, with limitations to the reaction rate from O_3 diffusion, Eq (11) & (12) predictions do not agree quantitatively with experimental observations or our explicit simulations (Fig. 4). The resistor model predicts faster kinetics than are observed or simulated (with predicted $\gamma \sim 1 \times 10^{-5}$), whereas fits using Eq. (11) by Dennis-Smither *et al*.[31] yielded values that are ~2x smaller (γ = 4-6 x 10^{-6}). This difference persists across observations that range in water content and MA concentration from 54 – 72% humidity (Table 3).

Both aqueous organic acid systems examined here are dominated by bulk-phase reactions with O_3, and show evidence in the shape of their observed and predicted decay kinetics for O_3 transport limitation. In Section 4.3, we explore how coupled adsorption, desorption, solvation, desolvation and diffusion processes control the overall rate of these bulk-dominated multiphase reactions.

4.2 Multiphase reaction of ozone with aqueous sodium nitrite. Next, we examine the multiphase oxidation of nitrite (NO_2^-) to nitrate (NO_3^-) by O_3, using our model framework of O_3 partitioning. Nitrite is both a faster-reacting and more surface-active species than the two organic acids discussed above, and thus provides an informative contrasting case. We use experimental results reported by Hunt *et al*.[91] for the reaction of O_3 with an aqueous nitrite particle (Fig. 5), where the decay of nitrite in optically trapped single particles was monitored using Raman spectroscopy. In their analysis, Hunt *et al*.[91] fit the NO_2^-

signal decay to the resistor model shown in Eq. (11). Using the diffusion coefficient and Henry's law constant for O_3 they extracted a rate coefficient for NO_2^- + O_3 from the fit, which provided a value consistent with previous bulk laboratory kinetic measurements.[93-97] This analysis implied that surface reactions, which are neglected in Eq. (11), were not required for describing the multiphase reaction rate of NO_2^- + O_3. Here, we use our predictive kinetic model to re-examine this result.

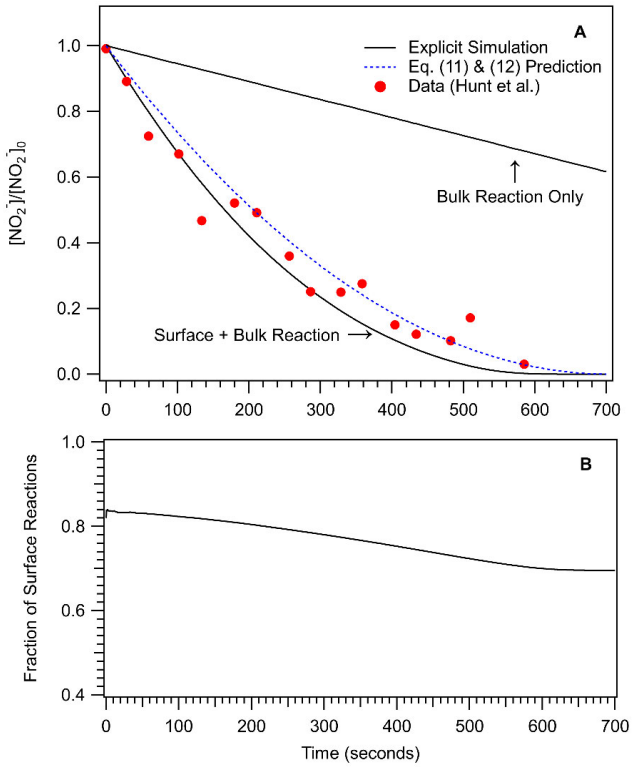

Figure 5: Normalized **(A)** $[NO_2^-]$ and **(B)** surface reaction fraction as a function of reaction time. Experiments are conducted using $[O_3]$ ~ 12 ppm_v, an 11.5 µm diameter aqueous droplet with an initial $[NO_2^-]$ = 0.2 mol L^{-1} as reported by Hunt *et al.* (see Table S4, Droplet 0).[91] The experimental conditions are used as inputs to the explicit simulation (black lines) as well as for the resistor model prediction (blue line), and both model predictions are generated using the same kinetic and thermodynamic parameters. See Table S3 for elementary steps and corresponding rate coefficients included in these simulations.

To explore the kinetic processes governing reaction timescales for NO_2^- + O_3, we first apply a modified version of our explicit kinetic model that assumes no surface reactions occur (Fig. 5a). We use a bulk reaction rate coefficient (5.6 x 10^{-16} cm^3 $molecule^{-1}$ s^{-1}) that is consistent with the measurements reported by Garland *et al.*,[95] and within the experimental uncertainty of the value reported by Hoigne *et al*[98] (Table S3 shows elementary reaction and diffusion steps). The impact of ionic strength on the magnitude of this rate coefficient (28 – 56 %, for the experimental particle concentrations reported by Hunt *et al.*[91]) is smaller than the experimental uncertainty in previously reported bulk-phase rate

coefficients (i.e., a factor of 2). For the $NaNO_2$ concentrations reported by Hunt *et al.*,[91] the effect of ionic strength on the magnitude of the O_3 Henry's Law constant is <5%.[26, 71] We assume that nitrite and nitrate diffusion coefficients in water are similar, and are taken from Yeh *et al.*[99]

Our simulations demonstrate that surface reactions contribute significantly to NO_2^- decay. Unlike the diffusion-limited bulk reaction resistor prediction using Eq. (11), our explicit model assuming only bulk processes predicts a nitrite decay that is 5-times slower than the observations, which suggests that the reaction timescales in this system are not driven entirely by bulk reaction. The difference between our bulk-only simulation and experimental observations is larger than the uncertainty in the bulk phase rate coefficients, suggesting that surface reactions are important to include under the experimental conditions reported by Hunt *et al.*[91] To include elementary steps at the interface, we assume that the interfacial rate coefficient for oxidation of nitrite by ozone is the same as that in the bulk (step S3 Table S3), and estimate values for the nitrite and nitrate bulk-interface partitioning equilibrium constant.

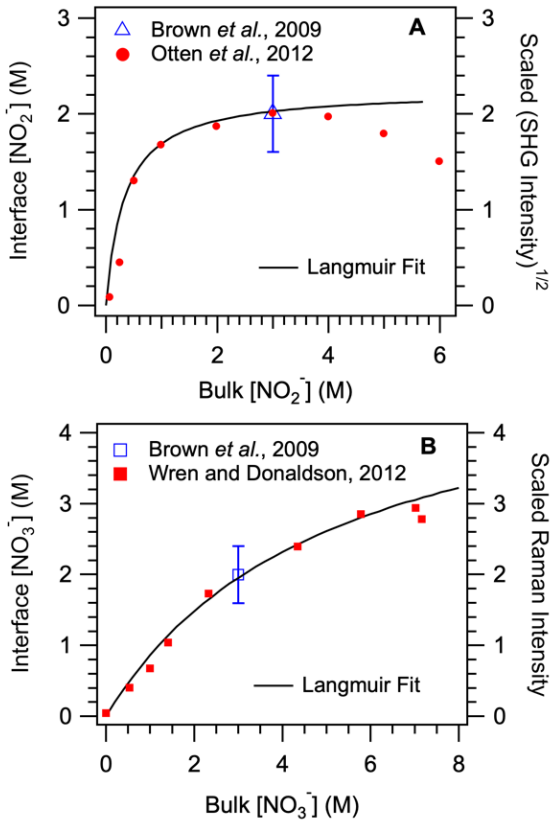

Figure 6 . Interfacial concentration of **(A)** NO_2^- and **(B)** NO_3^- vs bulk concentration derived from prior literature observations.[100-102]

The interfacial partitioning of anions, in particular nitrate, has been somewhat controversial with experiments and simulations arriving at different conclusions.[100, 101, 103-108] We briefly discuss available literature on this topic, in order to constrain the solvation and desolvation rate coefficients for nitrite and nitrate. Brown *et al,*[101] used X-ray photoemission to quantify the interfacial concentration of NO_2^- and NO_3^- in a liquid jet. At a bulk concentration of 3 M, the interfacial concentration, over the probing depth of the method, was 2 ± 0.4 M [101] indicating that although both ions reside near the interface (ca. 1.2 to 1.5 nm), their adsorbed concentrations are depleted relative to the bulk solution (2 vs. 3 M, Fig. 6a). Otten *et al.*[102] used Second-Harmonic Generation (SHG) spectroscopy to measure an adsorption isotherm for nitrite and found evidence for substantial surface partitioning and saturation. The square root of the SHG signal vs. bulk [NO_2^-] measured by Otten *et al.*[102] is shown in Fig. 6a. We scale the SHG signal to achieve the correct interfacial concentration observed by Brown *et al.,*[101] and fit the scaled data the Langmuir equation,

$$[NO_2^-]_{ads} = \frac{\Gamma_\infty^{NO_2^-}}{\delta} \cdot \frac{K_{eq}^{NO2-} \cdot [NO_2^-]_{bulk}}{1 + K_{eq}^{NO2-} \cdot [NO_2^-]_{bulk}} \quad \text{Eq. (13)}$$

where,

$$K_{eq}^{NO2-} = \frac{k_{desolv}}{k_{solv}} \quad \text{Eq. (14)}$$

to obtain K_{eq}^{NO2-} = 3.01 L mol^{-1} (5.0 x 10^{-21} cm^3 molec.$^{-1}$) and a maximum interface concentration ($\frac{\Gamma_\infty^{NO_2^-}}{\delta}$) of 2.25 M (1.35 x 10^{21} molec. cm^{-3}). K_{eq}^{NO2-} constrains the ratio of the desolvation (forward) and solvation (backward) rate coefficients for NO_2^- (Table S3, step S4). Our simulation results are insensitive to the absolute magnitude of these forward and backward rates over a broad range; for example the simulation results are the same when using values for the adsorption and desorption rate constants that are each a factor of 10^3 smaller than those shown in Table S3.

Evidence to date suggests[100, 108] that unlike nitrite, nitrate is only weakly adsorbed to the aqueous interface. To constrain this equilibrium, we use the nitrate adsorption isotherm measured by Wren and Donaldson[100] using glancing incidence Raman spectroscopy. In Fig. 6b, we show these measurements and scale the Raman intensity to the interfacial concentration observed by Brown *et al.*[101] A fit of this scaled data to the Langmuir isotherm yields K_{eq}^{NO3-} = 0.19 L mol^{-1} (3 x 10^{-22} cm^3 molec.$^{-1}$) and $\frac{\Gamma_\infty^{NO_2^-}}{\delta}$ = 5.3 M (3.2 x 10^{21} molec. cm^3). K_{eq}^{NO3-} is the same as that reported by Wren and Donaldson[100] using the same analysis

and within the estimates reported by Otten *et al.*[108] K_{eq}^{NO3-} is used in the equilibrium in step S5 (Table S3). As for nitrite, our simulation results are insensitive to the absolute magnitude of these forward and backward rates; for example simulation results are the same when using values that are a factor of 10^3 smaller from those shown in Table S3.

From the Langmuir fits for nitrite and nitrate, we see that NO_2^- is an order of magnitude more strongly partitioned to the interface than NO_3^-, which is reasonably consistent with prior observations. This implies that NO_3^- will not compete significantly with NO_2^- for sites at the interface. The reason for the factor of 3 difference in Γ_∞ for these two ions is unclear and may suggest ion pairing as described by Otten *et al*.[102] While the mechanism of anion adsorption to aqueous interfaces is not fully understood, the analysis above attempts to provide an experimentally constrained set of parameters for quantitative modeling of NO_2^- partitioning and reaction at the aqueous interface.

Our explicit simulation with both bulk and interfacial reactions predicts the NO_2^- reaction timescales observed by Hunt *et al*[91] (Fig. 5 & 7). Our explicit simulation is insensitive to the magnitude of the O_3 sticking coefficient (Fig. S11), so we use a conservative estimate of $\sigma = 10^{-4}$ in our simulation. Our explicit simulations demonstrate that although $[NO_2^-{}_{(ads)}]$ is depleted relative to the corresponding bulk concentration, under the experimental conditions used by Hunt *et al*. (Table S4),[91] 83 % of $O_3 + NO_2^-$ reactions occur at the interface over at the beginning of the reaction (Fig. 5b). As the NO_2^- concentration decreases, the fraction of surface reactions decreases toward 70%. Compared to AA and MA, the larger importance of interfacial reactions occurs due to a combination of a larger bimolecular rate coefficient for reaction with ozone, and the relatively larger adsorbed nitrite concentration. The dominance of surface reactions suggests that agreement between experimental kinetics and Eq (11) & (12) predictions (Fig. 5A, blue dashed line) arises for the wrong mechanistic reasons. Unlike the organic systems examined above, both predicted and observed decay kinetics appear more exponential in shape (Fig. 5 & 7). This suggests that O_3 transport is not limiting the multiphase reaction kinetics in this system, which is consistent with a surface-dominated reaction not limited by bulk O_3 diffusion.

Overall, this model-observation comparison demonstrates that our kinetic framework can represent the timescales of multiphase ozone reactions across multiple systems with differing physical and chemical properties. In the next section, we explore the coupled kinetic processes that control the multiphase reaction rate across these three systems.

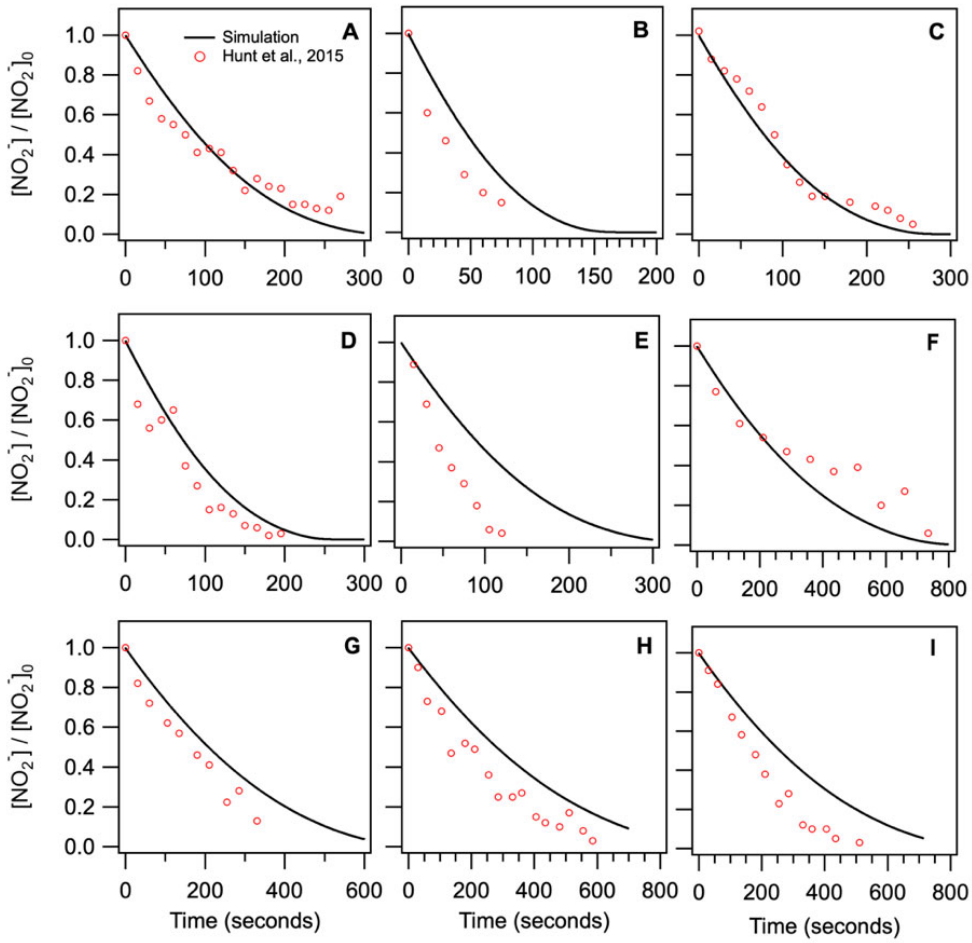

Figure 7. Decay of aqueous nitrite via multiphase reaction with ozone in micron-sized particles. Normalized nitrite concentration vs. time is shown for experiments (points) compared with explicit model predictions (lines). The experimental conditions for each droplet are shown in Table S4. The simulations are initialized with the experimental $[NO_2^-]$ and $[O_{3(g)}]$ reported by Hunt *et al.*[91] The panels correspond to: **(A)** Droplet 1 **(B)** Droplet 2 **(C)** Droplet 3, **(D)** Droplet 4, **(E)** Droplet 5, **(F)** Droplet 6, **(G)** Droplet 7, **(H)** Droplet 8, and **(I)** Droplet 9.

4.3 The impact of reaction on coupled O_3 partitioning kinetics and diffusion. To better understand the processes that govern ozone multiphase reaction timescales, we use a set of simulations that resolve the bulk ($[O_{3(b)}]$) and adsorbed ($[O_{3(ads)}]$) ozone concentrations for the initial experimental reaction conditions shown in Fig. 8. Further, we vary initial solute concentrations over a range corresponding to sub-saturated to super-saturated initial conditions (Fig. 9), or early to late reaction times, to examine the effects of changing the chemical lifetime on the balance between O_3 transport and bimolecular reaction. Since AA and MA behave similarly (dominance of bulk reaction (Section 4.1)), we use AA as a representative case. The selection frequencies of O_3 adsorption, desorption, solvation, desolvation and diffusion steps from these stochastic simulations (Fig. 9 & S13) illustrate how the relative importance of pairs of forward and reverse kinetic steps vary with droplet solute concentration.

In all three multiphase systems, $[O_{3(b)}]$ is depleted from its Henry's Law concentration, though to differing extents (Fig. 8 & 9). NO_2^- droplets are most strongly depleted relative to the Henry's Law ozone concentration, with $[O_{3(b)}] < 1\%$ of $H_{cc}^{gb}[O_{3(g)}]$. The organic acid droplets are depleted to lesser extents; $[O_{3(b)}]$ in the AA system is ~1% of $H_{cc}^{gb}[O_{3(g)}]$, while in the MA system O_3 is depleted to ~11% of its Henry's Law concentration. Both the AA and NO_2^- droplets approach the corresponding Henry's Law ozone concentration with decreasing initial solute concentration (Fig. 9), though the extent of bulk O_3 depletion at high solute concentrations differs significantly.

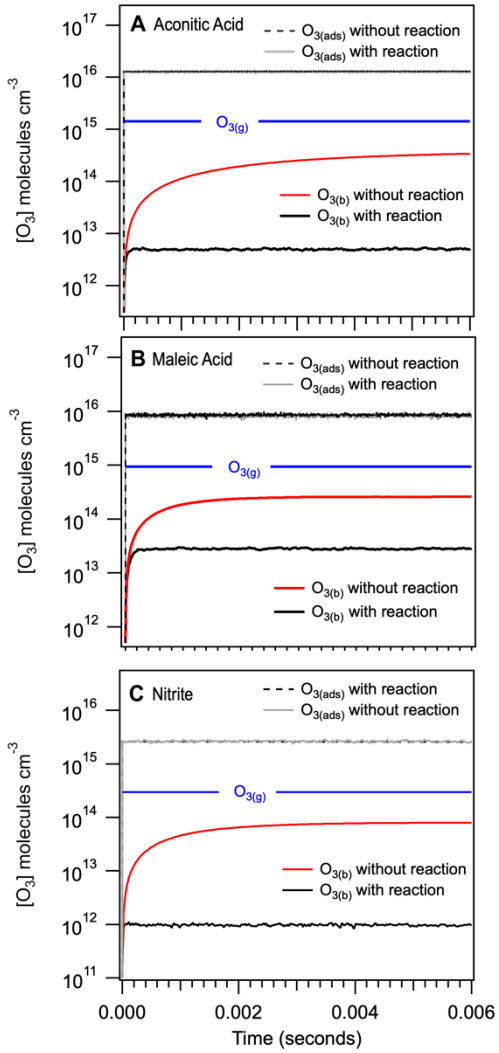

Figure 8: Simulated reactive uptake of O_3 to aqueous **(A)** *trans*-aconitic acid, **(B)** maleic acid, and **(C)** sodium nitrite droplets vs. time showing the partitioning of $O_{3(g)}$ to the interface and the bulk. Simulations are conducted with a steady state concentration of $O_{3(g)}$ and initial solute concentrations corresponding to experimental conditions (Fig. 3 (Experiment 1, $r_0 = 9.2$ μm), 4 (Droplet A, $r_0 = 4.6$ μm) and 5 (Droplet 0, $r_0 = 5.8$ μm)). Also shown in each panel are results from analogous simulations with no reactions.

The varying extents of bulk O_3 depletion are partially controlled by two factors that describe the balance between the timescales for O_3 diffusion and its reaction. First, the pseudo-first order rate coefficients for O_3 loss are a dominant driver of bulk O_3 depletion, such that the nitrite system is most strongly depleted and the maleic acid system is least depleted (i.e., $k_{rxn}[NO_2^-]_0 > k_{rxn}[AA]_0 > k_{rxn}[MA]_0$; Fig. 8). We emphasize that this trend is governed by both the magnitude of the second order rate coefficient and the solute concentration (determined by experimental relative humidity). Second, the droplet size differs across these three sets of experiments, such that the characteristic timescale for bulk ozone diffusion into these liquid particles differs. The diffusion timescale can be estimated as $\tau_{diffusion} = 1/k_{diffusion} = r^2/2D_{O3}$, such that $k_{diffusion,MA} > k_{diffusion,NO2-} > k_{diffusion,AA}$. We emphasize that this trend is driven by the experimental relative humidity and particle size (Tables 1, 3 and S4). Comparing the magnitudes of the rate coefficients for ozone diffusion with the pseudo-first order rate coefficients for O_3 consumption in the particle qualitatively explains the trends in $[O_{3(b)}]$ depletion, where MA is least depleted, followed by AA and with NO_2^- the most depleted (Fig. 8).

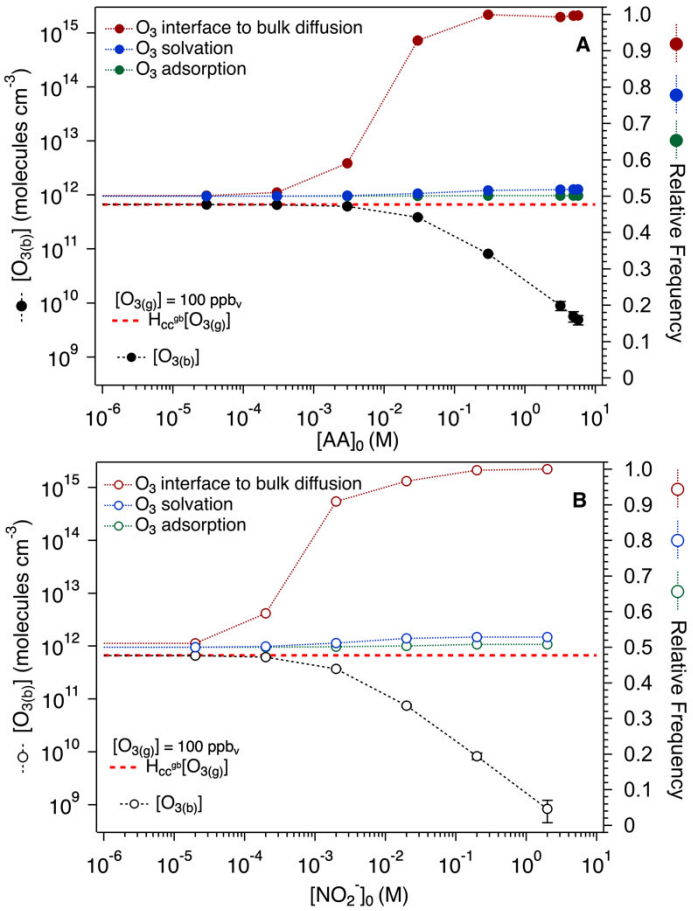

Figure 9: (Left axes) Simulated mean $[O_{3(b)}]$ for a wide range of simulated initial solution concentrations, for reactive uptake of O_3 to **(A)** *trans*-aconitic acid (AA, r_0 = 9.1 μm, solid circles) and **(B)** sodium nitrite (NO_2^-, r_0 =

5.8 μm, open circles) droplets at a steady state $[O_{3(g)}]$ = 100 ppb_v. The Henry's Law $[O_{3(b)}]$ is shown in the dashed red line. Error bars correspond to the standard deviation (i.e., stochastic variability) in simulated $[O_{3(b)}]$ over the first ~3 – 12 ms of reaction time, once $[O_{3(b)}]$ has equilibrated to a stable value (see Fig. 8). **(Right axes)** Simulated relative frequency of forward and reverse kinetics steps for O_3 (i.e., adsorption/desorption, solvation/desolvation and interface ↔ bulk diffusion) over the solute concentration range. Only forward kinetic steps are shown (interface to bulk diffusion, solvation and adsorption), as the fraction of reverse kinetic steps are their mirror image (Fig. S13).

For both AA and NO_2^-, $[O_{3(b)}]$ approaches its Henry's Law concentration (Fig. 9) only when the pseudo-first order rate coefficient for O_3 loss approaches the first-order rate coefficient for O_3 diffusion (i.e., $k_{rxn}[solute]_0 \approx k_{diffusion}$, where $[AA]_0$ = 44 mM and $[NO_2^-]_0$ = 2.8 mM). However, the solute concentration where diffusion and reaction timescales are equal ($k_{rxn}[solute]_0 = k_{diffusion}$) does not mark the onset of bulk O_3 depletion. Rather, this solute concentration lies within a regime where diffusion to and from the interface has already shifted significantly away from the non-reactive or dilute state, such that diffusion is occurring predominantly in one direction. In contrast, under dilute conditions O_3 rapidly equilibrates to both its bulk and interfacial Henry's Law concentrations (Fig. 8), and both diffusion and interfacial kinetic steps occur with equal frequency in both directions (Fig. 9 & S13). When diffusion and reaction timescales are equal, diffusion of solvated O_3 into the bulk accounts for ~90% of the total diffusion steps (Fig. 9). At experimental initial solute concentrations (i.e., < 100% relative humidity), diffusion proceeds only from just below the interface into the bulk. But, this maximum rate of O_3 delivery is not sufficient to compensate for the rate of O_3 reactive loss. Consequently, $[O_{3(b)}]$ becomes depleted from its Henry's Law concentration.

In addition to diffusion and reaction timescales, the thermodynamic properties of O_3 that govern gas-interface partitioning are a key component of our explicit kinetic model. While O_3 diffusion sets the transport rate for solvated O_3 to enter the particle bulk and become available for bulk reaction, non-reactive interfacial kinetic steps set the amount of adsorbed O_3 that is available to both become solvated and react at the interface. With and without reaction, and at all initial droplet concentrations ranging from molar to micromolar, $[O_{3(ads)}]$ is rapidly maintained (on a timescale of ~200 – 500 nanoseconds, Fig. 8 and Fig. S8) and remains constant given that $[O_{3(g)}]$ is constant. As initial solute concentrations increase, reactive loss of O_3 drives not only a shift in the dominant direction of diffusion steps, but also an increased frequency of O_3 solvation into the bulk and adsorption to the interface. This shift in the selection frequency, particularly in (de)solvation steps, is also apparent in the overall rate of each step as a function of reaction time (Fig. S14). These adjustments in the coupled O_3 partitioning equilibria maintain $[O_{3(ads)}]$, even though the rate of diffusion is unable to maintain $[O_{3(b)}]$ at high reaction rates. $[O_{3(ads)}]$ is maintained at its

interfacial Henry's Law concentration even for nitrite, where surface reactions are ~80% of all reaction events (Fig. 5b). Therefore, O_3 equilibration to the interface is fast relative to reactive loss in both the organic and inorganic systems examined here (Fig. S14), though this may not remain the case for faster-reacting solutes.

The overall response of the coupled O_3 partitioning and diffusion processes to reaction depends on the magnitude and location of the O_3 reactive loss. The dominant location of the O_3 reactive sink differs in the organic and inorganic systems (Sections 4.1 & 4.2), because solute interfacial affinity and reaction rates differ significantly. NO_2^- is the most surface active (i.e., $k_{desolv,NO_2^-}/k_{solv,NO_2^-} > k_{desolv,AA}/k_{solv,AA}$), has the largest bimolecular rate coefficient and exhibits the largest fraction of interfacial reactions. Consequently, the selection frequency of O_3 adsorption and desorption are impacted more strongly by a change in NO_2^- concentration than for a similar change in AA concentration (Fig. 9 and S13), though the magnitude of these changes are relatively small. Even though a majority of NO_2^- reactions occur at the interface, O_3 solvation and desolvation frequencies are forced to adjust in response to a change in $[NO_2^-]_0$ (Fig. 9 & S13) because O_3 diffusion from near the interface to the bulk cannot compensate for the rate of reactive loss. However, the dominance of surface reactions combined with the rapidly maintained $[O_{3(ads)}]$ avoids transport limitations and produces exponential-like kinetics for NO_2^- droplets (Fig. 5 & 7). For AA and MA, the majority of reactions occur in the bulk and the frequency of O_3 solvation and diffusion into the bulk are impacted by an increase in droplet solute concentration, while the adsorption response is almost negligible (Fig. 9 & S13). Despite the ample available adsorbed O_3, transport-limited (zeroth-order) kinetics arise for AA and MA at millimolar and higher concentrations, because the rate of diffusion away from the interface is too slow to compensate for reactive O_3 loss in the bulk.

The analysis above demonstrates that over the course of a multiphase reaction, coupled kinetic and diffusion steps dynamically respond and seek to maintain an equilibrium position that is achieved only at very low bimolecular reaction rates, or in the absence of reaction. In Section 4.1 and 4.2, we have compared our experimental observations and explicit model simulations to predictions from the diffusion-limited bulk reaction resistor model (Eq. (11) & (12), using the same kinetic and thermodynamic parameters as the explicit model), which is often applied to interpret the kinetics of multiphase reactions in micron-sized aqueous aerosol. However, this formulation overpredicts reaction rates for systems dominated by bulk reactions (AA and MA). We hypothesize that Eq. (11) & (12) effectively overpredicts the bulk O_3 concentration over the course of the reaction by assuming that O_3 partitioning is not coupled

to interfacial O_3 transport and diffusion away from the interface (i.e., Eq. (11) & (12) appear to assume that the reaction rate is modified by diffusion, while the bulk O_3 concentration is governed only by the Henry's Law constant). For surface reaction dominated systems (NO_2^-), Eq (11) & (12) are not mechanistically applicable even though the predicted reaction timescales agree with observations. Our results therefore suggest caution in applying the bulk O_3 diffusion limited resistor model to interpret multiphase reaction kinetics, especially when the contribution of surface and bulk reactions is not known. In a subsequent publication building on this and previous work,[16, 17, 109] we derive closed-form expressions for the bulk O_3 concentration and time-dependence of solute concentration during reaction, and will further examine the particle size-dependence of reactive O_3 uptake implied by rate-limiting diffusion processes.[110]

5. Conclusions

Using new and prior experimental measurements of reaction kinetics in micron-sized particles, we consider the multiphase reaction kinetics of ozone in three organic and inorganic systems (*trans*-aconitic acid, maleic acid and sodium nitrite) that have a range of interfacial affinities and bimolecular rate coefficients for reaction with ozone. We show that by representing ozone multiphase partitioning as a set of coupled kinetic and diffusion steps between gas, interface and bulk in a simple two-compartment model, we can accurately predict reaction timescales across all three systems. Our kinetic model is applicable within a range of solute concentrations where resistor model limiting cases are not applicable (i.e., $r_0/20 < L_{RD,O3} < r_0$), [21, 27] and in high solute concentration regimes relevant to aqueous aerosol (i.e., $L_{RD,O3} < r_0/20$) where bulk O_3 depletion arises through transport limitations. The model framework can capture interfacial and bulk kinetics across all three multiphase systems, but to do so it must explicitly account for the coupling of elementary O_3 partitioning steps with diffusion and reaction. These coupled kinetic processes rapidly maintain $[O_{3(ads)}]$ at the expense of $[O_{3(b)}]$ as a combination of solvated and adsorbed O_3 is lost to reaction. Despite important differences in solute interfacial concentrations across the three systems examined here, our kinetic model demonstrates that enhanced interfacial O_3 concentrations, compared to gas and bulk phases, are an important driver of the multiphase reaction timescale. This enhanced $[O_{3(ads)}]$ arises because of the free energy minimum at the interface implied by the magnitude of H_{cc}^{gs} (8.9), H_{cc}^{sb} (0.03) and associated free energies for O_3 adsorption and solvation.

We find that the relative importance of interfacial and bulk reactions depends on the surface affinity of both O_3 and the reacting solute, and the magnitude of the chemical lifetime. During the course

of a multiphase reaction, the coupled kinetic system dynamically seeks to maintain an equilibrium position that occurs only at millimolar and lower solute concentrations. For micron-sized multiphase reaction systems dominated by either bulk or interfacial reactions, transport limitations arise mainly due to the timescale for diffusion of solvated O_3 into the bulk. This diffusion limitation results in depletion of $[O_{3(b)}]$ from Henry's Law, which governs reaction timescales for slower-reacting, low surface activity species. For faster-reacting, more surface active species, the rapidly maintained $[O_{3(ads)}]$ allows interfacial reactions to proceed without significant transport limitation. In summary, our results demonstrate the importance of coupled reaction, diffusion and partitioning kinetics for setting the timescales of multiphase O_3 reactions.

Supporting Information

Figures S1-S14: Additional figures including details on the experimental set-up, product identification, model parameters, sensitivity and evaluation. Tables S1-S3: Kinetic and thermodynamic parameters used in the two-compartment model; Table S4: Experimental information for sodium nitrite droplets.

Acknowledgements

This work was supported by the Condensed Phase and Interfacial Molecular Science Program in the Chemical Sciences, Geosciences, and Biosciences Division of the Office of Basic Energy Sciences of the U.S. Department of Energy under Contract No. DEAC02-05CH11231. M.D.W. acknowledges a Natural Sciences and Engineering Research Council of Canada (NSERC) postdoctoral fellowship, which supported collection of experimental data used in this work. We thank Dr. Grazia Rovelli (LBNL) and Alex Prophet (LBNL) for many helpful discussions, Dr. Lance Lee (Stanford Research Systems) for the original design of the quadrupole electrodynamic trap, and Bruce Rude (LBNL) for technical support. We thank Professors Jonathan Reid (University of Bristol) and Martin King (Royal Holloway University of London) for providing previously published experimental data used in this work.

References

1. Poschl, U.; Shiraiwa, M., Multiphase Chemistry at the Atmosphere-Biosphere Interface Influencing Climate and Public Health in the Anthropocene. *Chemical Reviews* **2015,** *115* (10), 4440-4475.
2. Carslaw, K. S.; Boucher, O.; Spracklen, D. V.; Mann, G. W.; Rae, J. G. L.; Woodward, S.; Kulmala, M., A review of natural aerosol interactions and feedbacks within the Earth system. *Atmospheric Chemistry and Physics* **2010,** *10* (4), 1701-1737.
3. Abbatt, J. P. D.; Lee, A. K. Y.; Thornton, J. A., Quantifying trace gas uptake to tropospheric aerosol: recent advances and remaining challenges. *Chemical Society Reviews* **2012,** *41* (19), 6555-6581.
4. Zhou, S.; Hwang, B. C. H.; Lakey, P. S. J.; Zuend, A.; Abbatt, J. P. D.; Shiraiwa, M., Multiphase reactivity of polycyclic aromatic hydrocarbons is driven by phase separation and diffusion limitations. *Proc Natl Acad Sci U S A* **2019,** *116* (24), 11658-11663.

5. Shiraiwa, M.; Sosedova, Y.; Rouviere, A.; Yang, H.; Zhang, Y. Y.; Abbatt, J. P. D.; Ammann, M.; Poschl, U., The role of long-lived reactive oxygen intermediates in the reaction of ozone with aerosol particles. *Nature Chemistry* **2011,** *3* (4), 291-295.
6. Antinolo, M.; Willis, M. D.; Zhou, S. M.; Abbatt, J. P. D., Connecting the oxidation of soot to its redox cycling abilities. *Nature Communications* **2015,** *6*.
7. Finlayson-Pitts, B. J.; Wingen, L. M.; Perraud, V.; Ezell, M. J., Open questions on the chemical composition of airborne particles. *Communications Chemistry* **2020,** *3* (1).
8. Lohmann, U.; Feichter, J., Global indirect aerosol effects: a review. *Atmospheric Chemistry and Physics* **2005,** *5*, 715-737.
9. Jimenez, J. L.; Canagaratna, M. R.; Donahue, N. M.; Prevot, A. S. H.; Zhang, Q.; Kroll, J. H.; DeCarlo, P. F.; Allan, J. D.; Coe, H.; Ng, N. L.; Aiken, A. C.; Docherty, K. S.; Ulbrich, I. M.; Grieshop, A. P.; Robinson, A. L.; Duplissy, J.; Smith, J. D.; Wilson, K. R.; Lanz, V. A.; Hueglin, C.; Sun, Y. L.; Tian, J.; Laaksonen, A.; Raatikainen, T.; Rautiainen, J.; Vaattovaara, P.; Ehn, M.; Kulmala, M.; Tomlinson, J. M.; Collins, D. R.; Cubison, M. J.; Dunlea, E. J.; Huffman, J. A.; Onasch, T. B.; Alfarra, M. R.; Williams, P. I.; Bower, K.; Kondo, Y.; Schneider, J.; Drewnick, F.; Borrmann, S.; Weimer, S.; Demerjian, K.; Salcedo, D.; Cottrell, L.; Griffin, R.; Takami, A.; Miyoshi, T.; Hatakeyama, S.; Shimono, A.; Sun, J. Y.; Zhang, Y. M.; Dzepina, K.; Kimmel, J. R.; Sueper, D.; Jayne, J. T.; Herndon, S. C.; Trimborn, A. M.; Williams, L. R.; Wood, E. C.; Middlebrook, A. M.; Kolb, C. E.; Baltensperger, U.; Worsnop, D. R., Evolution of Organic Aerosols in the Atmosphere. *Science* **2009,** *326* (5959), 1525-1529.
10. Carlton, A. G.; Turpin, B. J., Particle partitioning potential of organic compounds is highest in the Eastern US and driven by anthropogenic water. *Atmospheric Chemistry and Physics* **2013,** *13* (20), 10203-10214.
11. Carlton, A. G.; Christiansen, A. E.; Flesch, M. M.; Hennigan, C. J.; Sareen, N., Mulitphase Atmospheric Chemistry in Liquid Water: Impacts and Controllability of Organic Aerosol. *Acc Chem Res* **2020,** *53* (9), 1715-1723.
12. Wilson, K. R.; Smith, J. D.; Kessler, S. H.; Kroll, J. H., The statistical evolution of multiple generations of oxidation products in the photochemical aging of chemically reduced organic aerosol. *Phys Chem Chem Phys* **2012,** *14* (4), 1468-79.
13. Heine, N.; Houle, F. A.; Wilson, K. R., Connecting the Elementary Reaction Pathways of Criegee Intermediates to the Chemical Erosion of Squalene Interfaces during Ozonolysis. *Environmental Science & Technology* **2017,** *51* (23), 13740-13748.
14. Houle, F. A.; Wiegel, A. A.; Wilson, K. R., Changes in Reactivity as Chemistry Becomes Confined to an Interface. The Case of Free Radical Oxidation of C30H62 Alkane by OH. *Journal of Physical Chemistry Letters* **2018,** *9* (5), 1053-1057.
15. Berkemeier, T.; Mishra, A.; Mattei, C.; Huisman, A. J.; Krieger, U. K.; Pöschl, U., Ozonolysis of Oleic Acid Aerosol Revisited: Multiphase Chemical Kinetics and Reaction Mechanisms. *ACS Earth and Space Chemistry* **2021,** *5* (12), 3313-3323.
16. Schwartz, S. E. In *Mass-Transport Considerations Pertinent to Aqueous Phase Reactions of Gases in Liquid-Water Clouds*, Chemistry of Multiphase Atmospheric Systems, Berlin, Heidelberg, 1986//; Jaeschke, W., Ed. Springer Berlin Heidelberg: Berlin, Heidelberg, 1986; pp 415-471.
17. Sander, R., Modeling Atmospheric Chemistry: Interactions between Gas-Phase Species and Liquid Cloud/Aerosol Particles. *Surveys in Geophysics* **1999,** *20* (1), 1-31.
18. Herrmann, H.; Schaefer, T.; Tilgner, A.; Styler, S. A.; Weller, C.; Teich, M.; Otto, T., Tropospheric Aqueous-Phase Chemistry: Kinetics, Mechanisms, and Its Coupling to a Changing Gas Phase. *Chemical Reviews* **2015,** *115* (10), 4259-4334.
19. Kolb, C. E.; Cox, R. A.; Abbatt, J. P. D.; Ammann, M.; Davis, E. J.; Donaldson, D. J.; Garrett, B. C.; George, C.; Griffiths, P. T.; Hanson, D. R.; Kulmala, M.; McFiggans, G.; Poschl, U.; Riipinen, I.; Rossi, M. J.; Rudich, Y.; Wagner, P. E.; Winkler, P. M.; Worsnop, D. R.; O' Dowd, C. D., An overview of current issues in the uptake of atmospheric trace gases by aerosols and clouds. *Atmospheric Chemistry and Physics* **2010,** *10* (21), 10561-10605.
20. Nathanson, G. M.; Davidovits, P.; Worsnop, D. R.; Kolb, C. E., Dynamics and kinetics at the gas-liquid interface. *Journal of Physical Chemistry* **1996,** *100* (31), 13007-13020.

21. Worsnop, D. R.; Morris, J. W.; Shi, Q.; Davidovits, P.; Kolb, C. E., A chemical kinetic model for reactive transformations of aerosol particles. *Geophysical Research Letters* **2002,** *29* (20).
22. Vacha, R.; Slavicek, P.; Mucha, M.; Finlayson-Pitts, B. J.; Jungwirth, P., Adsorption of Atmospherically Relevant Gases at the Air/Water Interface: Free Energy Profiles of Aqueous Solvation of N2, O2, O3, OH, H2O, HO2, and H2O2. *J Phys Chem A* **2004,** *108*, 11573-11579.
23. Vieceli, J.; Roeselova, M.; Potter, N.; Dang, L. X.; Garrett, B. C.; Tobias, D. J., Molecular Dynamics Simulations of Atmospheric Oxidants at the Air-Water Interface: Solvation and Accommodation of OH and O3. *J Phys Chem B* **2005,** *109*, 15876-15892.
24. Li, W.; Pak, C. Y.; Tse, Y.-L. S., Free energy study of H2O, N2O5, SO2, and O3 gas sorption by water droplets/slabs. *The Journal of Chemical Physics* **2018,** *148* (16), 164706.
25. Anglada, J. M.; Martins-Costa, M.; Ruiz-Lopez, M. F.; Francisco, J. S., Spectroscopic signatures of ozone at the air-water interface and photochemistry implications. *Proc Natl Acad Sci U S A* **2014,** *111* (32), 11618-23.
26. Danckwerts, P. V., *Gas-liquid reactions*. John Wiley & Sons, Ltd: 1971; p 509-510.
27. Smith, G. D.; Woods, E.; DeForest, C. L.; Baer, T.; Miller, R. E., Reactive Uptake of Ozone by Oleic Acid Aerosol Particles: Application of Single-Particle Mass Spectrometry to Heterogeneous Reaction Kinetics. *J Phys Chem A* **2002,** (106), 8085-8095.
28. Berkemeier, T.; Huisman, A. J.; Ammann, M.; Shiraiwa, M.; Koop, T.; Poschl, U., Kinetic regimes and limiting cases of gas uptake and heterogeneous reactions in atmospheric aerosols and clouds: a general classification scheme. *Atmospheric Chemistry and Physics* **2013,** *13* (14), 6663-6686.
29. Ravishankara, A. R., Heterogeneous and multiphase chemistry in the troposphere. *Science* **1997,** *276* (5315), 1058-1065.
30. Smith, G. D.; Woods, E.; Baer, T.; Miller, R. E., Aerosol Uptake Described by Numerical Solution of the Diffusion−Reaction Equations in the Particle. *The Journal of Physical Chemistry A* **2003,** *107* (45), 9582-9587.
31. Dennis-Smither, B. J.; Marshall, F. H.; Miles, R. E.; Preston, T. C.; Reid, J. P., Volatility and oxidative aging of aqueous maleic acid aerosol droplets and the dependence on relative humidity. *J Phys Chem A* **2014,** *118* (30), 5680-91.
32. Davidovits, P.; Kolb, C. E.; Williams, L. R.; Jayne, J. T.; Worsnop, D. R., Mass accommodation and chemical reactions at gas-liquid interfaces. *Chemical Reviews* **2006,** *106* (4), 1323-1354.
33. Arangio, A. M.; Slade, J. H.; Berkemeier, T.; Poschl, U.; Knopf, D. A.; Shiraiwa, M., Multiphase Chemical Kinetics of OH Radical Uptake by Molecular Organic Markers of Biomass Burning Aerosols: Humidity and Temperature Dependence, Surface Reaction, and Bulk Diffusion. *Journal of Physical Chemistry A* **2015,** *119* (19), 4533-4544.
34. Berkemeier, T.; Steimer, S. S.; Krieger, U. K.; Peter, T.; Poschl, U.; Ammann, M.; Shiraiwa, M., Ozone uptake on glassy, semi-solid and liquid organic matter and the role of reactive oxygen intermediates in atmospheric aerosol chemistry. *Phys Chem Chem Phys* **2016,** *18* (18), 12662-74.
35. Shiraiwa, M.; Pfrang, C.; Koop, T.; Pöschl, U., Kinetic multi-layer model of gas-particle interactions in aerosols and clouds (KM-GAP): linking condensation, evaporation and chemical reactions of organics, oxidants and water. *Atmospheric Chemistry and Physics* **2012,** *12* (5), 2777-2794.
36. Roldin, P.; Eriksson, A. C.; Nordin, E. Z.; Hermansson, E.; Mogensen, D.; Rusanen, A.; Boy, M.; Swietlicki, E.; Svenningsson, B.; Zelenyuk, A.; Pagels, J., Modelling non-equilibrium secondary organic aerosol formation and evaporation with the aerosol dynamics, gas- and particle-phase chemistry kinetic multilayer model ADCHAM. *Atmospheric Chemistry and Physics* **2014,** *14* (15), 7953-7993.
37. Shiraiwa, M.; Pfrang, C.; Pöschl, U., Kinetic multi-layer model of aerosol surface and bulk chemistry (KM-SUB): the influence of interfacial transport and bulk diffusion on the oxidation of oleic acid by ozone. *Atmos. Chem. Phys.* **2010,** *10* (8), 3673-3691.
38. Steimer, S. S.; Berkemeier, T.; Gilgen, A.; Krieger, U. K.; Peter, T.; Shiraiwa, M.; Ammann, M., Shikimic acid ozonolysis kinetics of the transition from liquid aqueous solution to highly viscous glass. *Phys Chem Chem Phys* **2015,** *17* (46), 31101-9.
39. Marshall, F. H.; Berkemeier, T.; Shiraiwa, M.; Nandy, L.; Ohm, P. B.; Dutcher, C. S.; Reid, J. P., Influence of particle viscosity on mass transfer and heterogeneous ozonolysis kinetics in aqueous-sucrose-maleic acid aerosol. *Phys Chem Chem Phys* **2018,** *20* (22), 15560-15573.

40. DeRieux, W.-S. W.; Lakey, P. S. J.; Chu, Y.; Chan, C. K.; Glicker, H. S.; Smith, J. N.; Zuend, A.; Shiraiwa, M., Effects of Phase State and Phase Separation on Dimethylamine Uptake of Ammonium Sulfate and Ammonium Sulfate–Sucrose Mixed Particles. *ACS Earth and Space Chemistry* **2019,** *3* (7), 1268-1278.
41. Houle, F. A.; Wiegel, A. A.; Wilson, K. R., Predicting Aerosol Reactivity Across Scales: from the Laboratory to the Atmosphere. *Environ Sci Technol* **2018,** *52* (23), 13774-13781.
42. Wiegel, A. A.; Wilson, K. R.; Hinsberg, W. D.; Houle, F. A., Stochastic methods for aerosol chemistry: a compact molecular description of functionalization and fragmentation in the heterogeneous oxidation of squalane aerosol by OH radicals. *Physical Chemistry Chemical Physics* **2015,** *17* (6), 4398-4411.
43. Hinsberg, W. D.; Houle, F. A., Kineticope ©. *https://hinsberg.net/kinetiscope/* **2020**.
44. Houle, F. A.; Hinsberg, W. D.; Wilson, K. R., Oxidation of a model alkane aerosol by OH radical: the emergent nature of reactive uptake. *Physical Chemistry Chemical Physics* **2015,** *17* (6), 4412-4423.
45. Zeng, M.; Wilson, K. R., Efficient Coupling of Reaction Pathways of Criegee Intermediates and Free Radicals in the Heterogeneous Ozonolysis of Alkenes. *J Phys Chem Lett* **2020,** *11* (16), 6580-6585.
46. Zeng, M.; Heine, N.; Wilson, K. R., Evidence that Criegee intermediates drive autoxidation in unsaturated lipids. *Proceedings of the National Academy of Sciences* **2020,** *117* (9), 4486-4490.
47. Liu, M. J.; Wiegel, A. A.; Wilson, K. R.; Houle, F. A., Aerosol Fragmentation Driven by Coupling of Acid-Base and Free-Radical Chemistry in the Heterogeneous Oxidation of Aqueous Citric Acid by OH Radicals. *Journal of Physical Chemistry A* **2017,** *121* (31), 5856-5870.
48. Davies, J. F.; Wilson, K. R., Nanoscale interfacial gradients formed by the reactive uptake of OH radicals onto viscous aerosol surfaces. *Chemical Science* **2015,** *6* (12), 7020-7027.
49. Lee, L.; Wilson, K., The Reactive-Diffusive Length of OH and Ozone in Model Organic Aerosols. *Journal of Physical Chemistry A* **2016,** *120* (34), 6800-6812.
50. Willis, M. D.; Rovelli, G.; Wilson, K. R., Combining mass spectrometry of picoliter samples with a multi-compartment electrodynamic trap for probing the chemistry of droplet arrays. *Anal Chem* **2020**.
51. Jacobs, M. I.; Davies, J. F.; Lee, L.; Davis, R. D.; Houle, F.; Wilson, K. R., Exploring Chemistry in Microcompartments Using Guided Droplet Collisions in a Branched Quadrupole Trap Coupled to a Single Droplet, Paper Spray Mass Spectrometer. *Analytical Chemistry* **2017,** *89* (22), 12511-12519.
52. Davies, J. F.; Haddrell, A. E.; Miles, R. E. H.; Bull, C. R.; Reid, J. P., Bulk, Surface, and Gas-Phase Limited Water Transport in Aerosol. *Journal of Physical Chemistry A* **2012,** *116* (45), 10987-10998.
53. Davies, J. F., Mass, Charge and Radius of Droplets in a Linear Quadrupole Electrodynamic Balance. *Aerosol Science and Technology* **2019**, 1-29.
54. Kaur Kohli, R.; Davies, J. F., Paper Spray Mass Spectrometry for the Analysis of Picoliter Droplets. *The Analyst* **2020**.
55. Kohli, R. K.; Davies, J. F., Measuring the Chemical Evolution of Levitated Particles: A Study on the Evaporation of Multicomponent Organic Aerosol. *Anal Chem* **2021,** *93* (36), 12472-12479.
56. Upton, K. T.; Schilling, K. A.; Beauchamp, J. L., Easily fabricated ion source for characterizing mixtures of organic compounds by direct analysis in real time mass spectrometry. *Analytical Methods* **2017,** *9* (34), 5065-5074.
57. Shelley, J. T.; Wiley, J. S.; Chan, G. C.; Schilling, G. D.; Ray, S. J.; Hieftje, G. M., Characterization of direct-current atmospheric-pressure discharges useful for ambient desorption/ionization mass spectrometry. *J Am Soc Mass Spectrom* **2009,** *20* (5), 837-44.
58. Rovelli, G.; Jacobs, M. I.; Willis, M. D.; Rapf, R. J.; Prophet, A. M.; Wilson, K. R., A critical analysis of electrospray techniques for the determination of accelerated rates and mechanisms of chemical reactions in droplets. *Chemical Science* **2020**.
59. Ammann, M.; Cox, R. A.; Crowley, J. N.; Jenkin, M. E.; Mellouki, A.; Rossi, M. J.; Troe, J.; Wallington, T. J., Evaluated kinetic and photochemical data for atmospheric chemistry: Volume VI - heterogeneous reactions with liquid substrates. *Atmospheric Chemistry and Physics* **2013,** *13* (16), 8045-8228.
60. Hanson, D. R., Surface-Specific Reactions on Liquids. *The Journal of Physical Chemistry B* **1997,** *101* (25), 4998-5001.
61. Remorov, R. G.; George, C., Analysis of chemical kinetics at the gas-aqueous interface for submicron aerosols. *Phys Chem Chem Phys* **2006,** *8* (42), 4897-901.

62. Bunker, D. L.; Garrett, B.; Kleindienst, T.; Long, G. S., Discrete simulation methods in combustion kinetics. *Combustion and Flame* **1974,** *23* (3), 373-379.
63. Gillespie, D. T., General Method for Numerically Simulating Stochastic Time Evolution of Coupled Chemical-Reactions. *Journal of Computational Physics* **1976,** *22* (4), 403-434.
64. Heine, N.; Arata, C.; Goldstein, A. H.; Houle, F. A.; Wilson, K. R., Multiphase Mechanism for the Production of Sulfuric Acid from SO2 by Criegee Intermediates Formed During the Heterogeneous Reaction of Ozone with Squalene. *Journal of Physical Chemistry Letters* **2018,** *9* (12), 3504-3510.
65. Wilson, K. R.; Prophet, A. M.; Rovelli, G.; Willis, M. D.; Rapf, R. J.; Jacobs, M. I., A kinetic description of how interfaces accelerate reactions in micro-compartments. *Chemical Science* **2020**.
66. Sander, R., Compilation of Henry's law constants (version 4.0) for water as solvent. *Atmospheric Chemistry and Physics* **2015,** *15* (8), 4399-4981.
67. Utter, R. G.; Burkholder, J. B.; Howard, C. J.; Ravishankara, A. R., Measurement of the mass accommodation coefficient of ozone on aqueous surfaces. *The Journal of Physical Chemistry* **1992,** *96* (12), 4973-4979.
68. Hu, J. H.; Shi, Q.; Davidovits, P.; Worsnop, D. R.; Zahniser, M. S.; Kolb, C. E., Reactive Uptake of Cl2(g) and Br2(g) by Aqueous Surfaces as a Function of Br- and I- Ion Concentration: The Effect of Chemical Reaction at the Interface. *The Journal of Physical Chemistry* **1995,** *99* (21), 8768-8776.
69. Magi, L.; Schweitzer, F.; Pallares, C.; Cherif, S.; Mirabel, P.; George, C., Investigation of the Uptake Rate of Ozone and Methyl Hydroperoxide by Water Surfaces. *The Journal of Physical Chemistry A* **1997,** *101* (27), 4943-4949.
70. Schütze, M.; Herrmann, H., Determination of phase transfer parameters for the uptake of HNO3, N2O5 and O3 on single aqueous drops. *Physical Chemistry Chemical Physics* **2002,** *4* (1), 60-67.
71. Müller, B.; Heal, M. R., The mass accommodation coefficient of ozone on an aqueous surface. *Physical Chemistry Chemical Physics* **2002,** *4* (14), 3365-3369.
72. Vereecken, L.; Harder, H.; Novelli, A., The reactions of Criegee intermediates with alkenes, ozone, and carbonyl oxides. *Phys Chem Chem Phys* **2014,** *16* (9), 4039-49.
73. Bleys, G.; Joos, P., Adsorption kinetics of bolaform surfactants at the air/water interface. *The Journal of Physical Chemistry* **1985,** *89* (6), 1027-1032.
74. Bidstrup, D. E.; Geankoplis, C. J., Aqueous Molecular Diffusivities of Carboxylic Acids. *Journal of Chemical & Engineering Data* **1963,** *8* (2), 170-173.
75. Gottschalk, C.; Libra, J. A.; Saupe, A., *Ozonation of Water and Waste Water: A Practical Guide to Understanding Ozone and its Applications*. 2 ed.; Wiley-VCH Verlag GmbH & Co.: 2010.
76. Leitzke, A.; Sonntag, C. v., Ozonolysis of Unsaturated Acids in Aqueous Solution: Acrylic, Methacrylic, Maleic, Fumaric and Muconic Acids. *Ozone: Science & Engineering* **2009,** *31* (4), 301-308.
77. Vereecken, L.; Novelli, A.; Taraborrelli, D., Unimolecular decay strongly limits the atmospheric impact of Criegee intermediates. *Phys Chem Chem Phys* **2017,** *19* (47), 31599-31612.
78. Zhou, S.; Joudan, S.; Forbes, M. W.; Zhou, Z.; Abbatt, J. P. D., Reaction of Condensed-Phase Criegee Intermediates with Carboxylic Acids and Perfluoroalkyl Carboxylic Acids. *Environmental Science & Technology Letters* **2019,** *6* (4), 243-250.
79. Zhou, Z.; Abbatt, J. P. D., Formation of Gas-Phase Hydrogen Peroxide via Multiphase Ozonolysis of Unsaturated Lipids. *Environmental Science & Technology Letters* **2020**.
80. Zuend, A.; Marcolli, C.; Booth, A. M.; Lienhard, D. M.; Soonsin, V.; Krieger, U. K.; Topping, D. O.; McFiggans, G.; Peter, T.; Seinfeld, J. H., New and extended parameterization of the thermodynamic model AIOMFAC: calculation of activity coefficients for organic-inorganic mixtures containing carboxyl, hydroxyl, carbonyl, ether, ester, alkenyl, alkyl, and aromatic functional groups. *Atmos. Chem. Phys.* **2011,** *11* (17), 9155-9206.
81. Wexler, A. S.; Clegg, S. L., Atmospheric aerosol models for systems including the ions H+, NH4+, Na+, SO42-, NO3-,Cl-, Br-, and H2O. *Journal of Geophysical Research-Atmospheres* **2002,** *107* (D14).
82. Clegg, S. L.; Seinfeld, J. H., Thermodynamic Models of Aqueous Solutions Containing Inorganic Electrolytes and Dicarboxylic Acids at 298.15 K. 2. Systems Including Dissociation Equilibria. *The Journal of Physical Chemistry A* **2006,** *110* (17), 5718-5734.

83. Pfendt, L.; Drazić, B.; Popović, G.; Drakulić, B.; Vitnik, Z.; Juranić, I., Determination of all pKa Values of Some di- and Tri-Carboxylic Unsaturated and Epoxy Acids and Their Polylinear Correlation with the Carboxylic Group Atomic Charges. *Journal of Chemical Research* **2003,** *2003* (5), 247-248.
84. Langmuir, I., The Adsorption of Gases on Plane Surfaces of Glass, Mica and Platinum. *Journal of the American Chemical Society* **1918,** *40* (9), 1361-1403.
85. Boyer, H. C.; Dutcher, C. S., Statistical Thermodynamic Model for Surface Tension of Aqueous Organic Acids with Consideration of Partial Dissociation. *The Journal of Physical Chemistry A* **2016,** *120* (25), 4368-4375.
86. Poschl, U.; Rudich, Y.; Ammann, M., Kinetic model framework for aerosol and cloud surface chemistry and gas-particle interactions – Part 1: General equations, parameters, and terminology. *Atmos Chem Phys* **2007,** *7*, 5989-6023.
87. Shi, Q.; Li, Y. Q.; Davidovits, P.; Jayne, J. T.; Worsnop, D. R.; Mozurkewich, M.; Kolb, C. E., Isotope Exchange for Gas-Phase Acetic Acid and Ethanol at Aqueous Interfaces: A Study of Surface Reactions. *The Journal of Physical Chemistry B* **1999,** *103* (13), 2417-2430.
88. Jayne, J. T.; Duan, S. X.; Davidovits, P.; Worsnop, D. R.; Zahniser, M. S.; Kolb, C. E., Uptake of gas-phase alcohol and organic acid molecules by water surfaces. *The Journal of Physical Chemistry* **1991,** *95* (16), 6329-6336.
89. Roeselová, M.; Jungwirth, P.; Tobias, D. J.; Gerber, R. B., Impact, Trapping, and Accommodation of Hydroxyl Radical and Ozone at Aqueous Salt Aerosol Surfaces. A Molecular Dynamics Study. *The Journal of Physical Chemistry B* **2003,** *107* (46), 12690-12699.
90. Engel, T.; Ertl, G., Surface Residence Times and Reaction Mechanism in the Catalytic Oxidation of Co on Pd(111). *Chemical Physics Letters* **1978,** *54* (1), 95-98.
91. Hunt, O. R.; Ward, A. D.; King, M. D., Heterogeneous oxidation of nitrite anion by gas-phase ozone in an aqueous droplet levitated by laser tweezers (optical trap): is there any evidence for enhanced surface reaction? *Physical Chemistry Chemical Physics* **2015,** *17* (4), 2734-2741.
92. Gallimore, P. J.; Achakulwisut, P.; Pope, F. D.; Davies, J. F.; Spring, D. R.; Kalberer, M., Importance of relative humidity in the oxidative ageing of organic aerosols: case study of the ozonolysis of maleic acid aerosol. *Atmospheric Chemistry and Physics* **2011,** *11* (23), 12181-12195.
93. Damschen, D. E.; Martin, L. R., Aqueous aerosol oxidation of nitrous acid by O2, O3 and H2O2. *Atmospheric Environment (1967)* **1983,** *17* (10), 2005-2011.
94. Hoigné, J.; Bader, H., Rate constants of reactions of ozone with organic and inorganic compounds in water—II: Dissociating organic compounds. *Water Research* **1983,** *17* (2), 185-194.
95. Garland, J. A.; Elzerman, A. W.; Penkett, S. A., The mechanism for dry deposition of ozone to seawater surfaces. *Journal of Geophysical Research: Oceans* **1980,** *85* (C12), 7488-7492.
96. Liu, Q.; Schurter, L. M.; Muller, C. E.; Aloisio, S.; Francisco, J. S.; Margerum, D. W., Kinetics and Mechanisms of Aqueous Ozone Reactions with Bromide, Sulfite, Hydrogen Sulfite, Iodide, and Nitrite Ions. *Inorganic Chemistry* **2001,** *40* (17), 4436-4442.
97. Penkett, S. A., Oxidation of SO2 and Other Atmospheric Gases by Ozone in Aqueous Solution. *Nature Physical Science* **1972,** *240* (101), 105-106.
98. Hoigné, J.; Bader, H.; Haag, W. R.; Staehelin, J., Rate constants of reactions of ozone with organic and inorganic compounds in water—III. Inorganic compounds and radicals. *Water Research* **1985,** *19* (8), 993-1004.
99. Yeh, H. S.; Wills, G. B., Diffusion coefficient of sodium nitrate in aqueous solution at 25.deg. as a function of concentration from 0.1 to 1.0M. *Journal of Chemical & Engineering Data* **1970,** *15* (1), 187-189.
100. Wren, S. N.; Donaldson, D. J., Glancing-angle Raman study of nitrate and nitric acid at the air–aqueous interface. *Chemical Physics Letters* **2012,** *522*, 1-10.
101. Brown, M. A.; Winter, B.; Faubel, M.; Hemminger, J. C., Spatial Distribution of Nitrate and Nitrite Anions at the Liquid/Vapor Interface of Aqueous Solutions. *Journal of the American Chemical Society* **2009,** *131* (24), 8354-8355.
102. Otten, D. E.; Onorato, R.; Michaels, R.; Goodknight, J.; Saykally, R. J., Strong surface adsorption of aqueous sodium nitrite as an ion pair. *Chemical Physics Letters* **2012,** *519-520*, 45-48.

103. Tian, C.; Byrnes, S. J.; Han, H.-L.; Shen, Y. R., Surface Propensities of Atmospherically Relevant Ions in Salt Solutions Revealed by Phase-Sensitive Sum Frequency Vibrational Spectroscopy. *The Journal of Physical Chemistry Letters* **2011,** *2* (15), 1946-1949.
104. Tobias, D. J.; Stern, A. C.; Baer, M. D.; Levin, Y.; Mundy, C. J., Simulation and Theory of Ions at Atmospherically Relevant Aqueous Liquid-Air Interfaces. *Annual Review of Physical Chemistry* **2013,** *64* (1), 339-359.
105. Dang, L. X.; Chang, T.-M.; Roeselova, M.; Garrett, B. C.; Tobias, D. J., On NO3−–H2O interactions in aqueous solutions and at interfaces. *The Journal of Chemical Physics* **2006,** *124* (6), 066101.
106. Salvador, P.; Curtis, J. E.; Tobias, D. J.; Jungwirth, P., Polarizability of the nitrate anion and its solvation at the air/water interface. *Physical Chemistry Chemical Physics* **2003,** *5* (17), 3752-3757.
107. Thomas, J. L.; Roeselová, M.; Dang, L. X.; Tobias, D. J., Molecular Dynamics Simulations of the Solution−Air Interface of Aqueous Sodium Nitrate. *The Journal of Physical Chemistry A* **2007,** *111* (16), 3091-3098.
108. Otten, D. E.; Petersen, P. B.; Saykally, R. J., Observation of nitrate ions at the air/water interface by UV-second harmonic generation. *Chemical Physics Letters* **2007,** *449* (4), 261-265.
109. Kumar, S., The characteristic time to achieve interfacial phase equilibrium in cloud drops. *Atmospheric Environment (1967)* **1989,** *23* (10), 2299-2304.
110. Wilson, K. R.; Prophet, A. M.; Willis, M. D., A Kinetic Model for Predicting Trace Gas Uptake and Reaction. In *ChemRxiv* *https://chemrxiv.org/engage/chemrxiv/article-details/62729c8359f0d6c6ce83a88a, DOI: 10.26434/chemrxiv-2022-m88b6*, 2022.

TOC Graphic

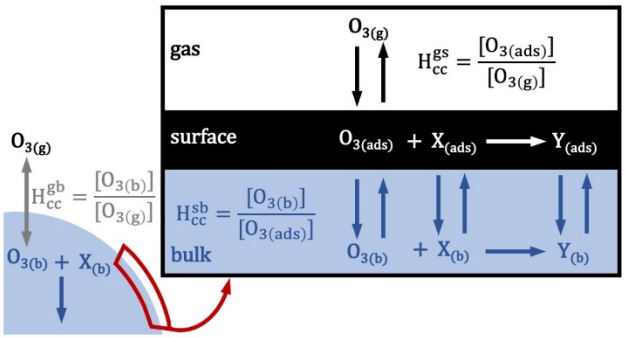
gas
$O_{3(g)}$
$H_{cc}^{gs} = \frac{[O_{3(ads)}]}{[O_{3(g)}]}$
surface
$O_{3(ads)} + X_{(ads)} \rightarrow Y_{(ads)}$
$O_{3(g)}$
$H_{cc}^{gb} = \frac{[O_{3(b)}]}{[O_{3(g)}]}$
$H_{cc}^{sb} = \frac{[O_{3(b)}]}{[O_{3(ads)}]}$
bulk
$O_{3(b)} + X_{(b)}$
$O_{3(b)}$
$+ X_{(b)}$
$Y_{(b)}$

Supplementary Information for

Coupled Interfacial and Bulk Kinetics Govern the Timescales of Multiphase Ozonolysis Reactions

Megan D. Willis[1] and Kevin R. Wilson[2]

[1]Department of Chemistry, Colorado State University, Fort Collins, CO, USA

[2]Chemical Sciences Division, Lawrence Berkeley National Lab, Berkeley, CA, USA

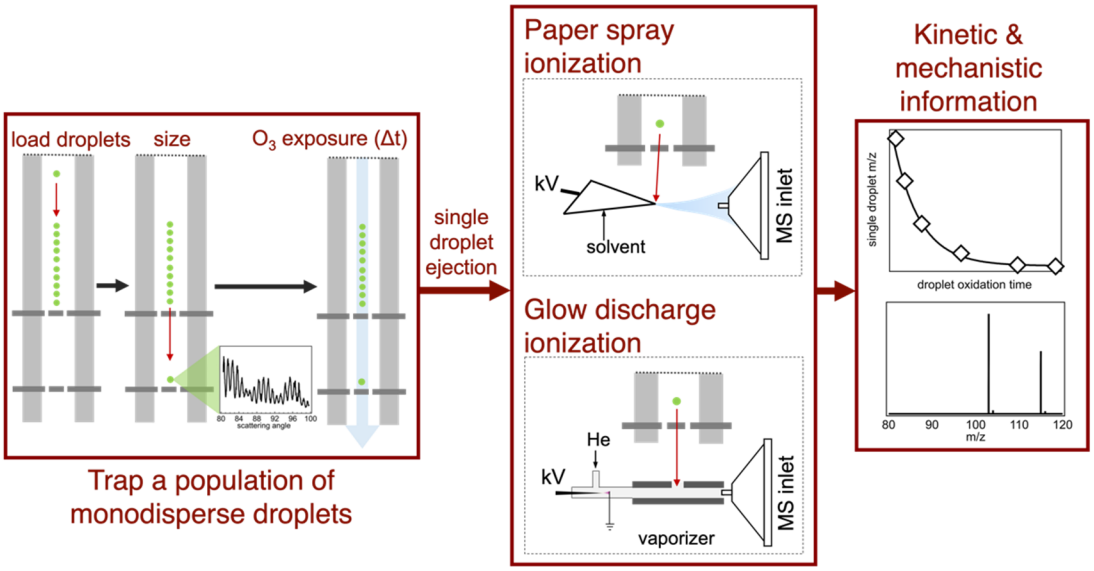

Figure S1: Schematic of the Quadrupole Electrodynamic Trap (QET) experimental procedure for ozonolysis experiments. A monodisperse population of droplets is first loaded into the QET, with constant humidity. Unreacted droplets are sized and their composition is measured with one of two possible ambient ionization sources. Remaining droplets are then exposed to ozone for a period of time, after which the ozone flow is switched off and a series of partially reacted single droplets are sized and ejected to obtain chemical information from mass spectrometry. Design and operation of the two ambient ionization sources for single droplets is described in Willis et al.[1] Kinetic and mechanistic information is obtained from the mass spectra of multiple (n> 8) single droplets. Thermal desorption glow discharge ionization is used for all kinetic data presented here, while paper spray ionization is used to confirm product assignments.

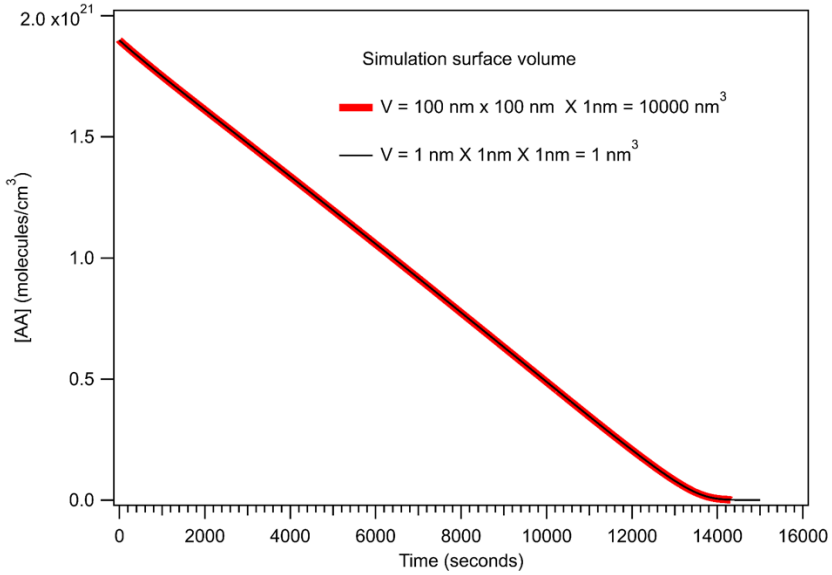

Figure S2. Decay of [AA] vs. time for two simulations geometries. Shown are simulations results for a 1 nm X 1 nm X r/3 nm rectangular prism compared with results from a 100 nm X 100 nm X r/3 nm prism. Results from both geometries are indistinguishable.

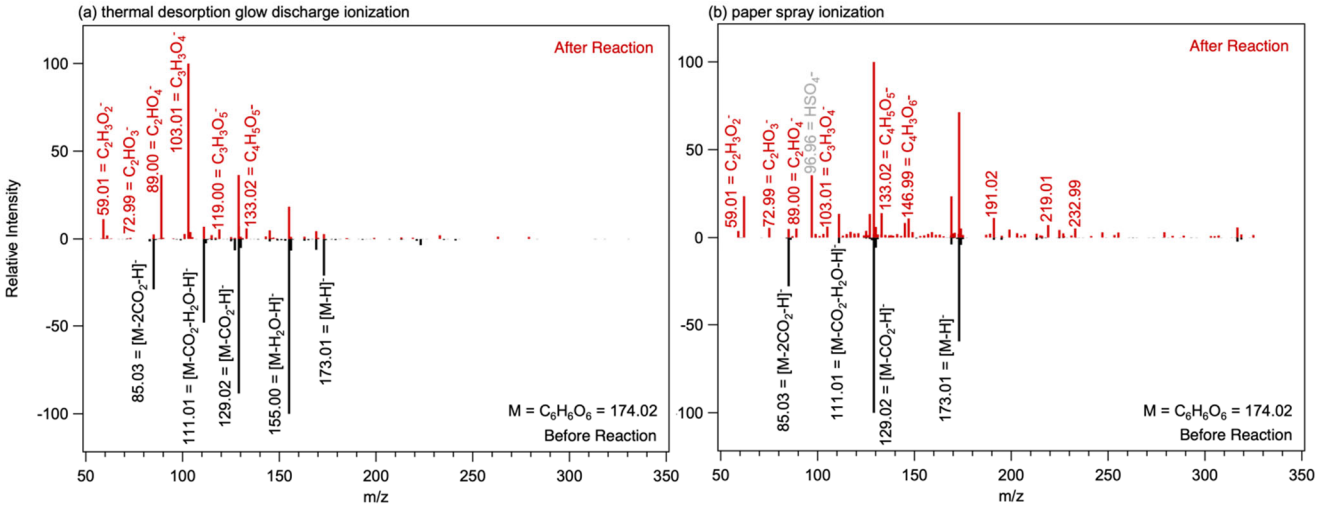

Figure S3: Representative mass spectra of trans-Aconitic Acid particles before reaction (black) and after reaction (red), measured by negative mode (a) thermal-desorption glow-discharge ionization mass spectrometry (TDGD-MS) and (b) paper spray ionization mass spectrometry (PS-MS). The appearance of HSO_4^- arises from decreased ion suppression as the reaction proceeds, as HSO_4^- is a prevalent peak observed in the paper spray background.[1] The expected major C_4 ketone product ($C_4H_3O_5^-$) is observable in most experiments, but at very low signal intensities. We observed of significant amount of fragmentation of the starting tri-acid with both ionization techniques, where both dehydration and decarboxylation are prevalent in TDGD-MS and decarboxylation is most prevalent with PSMS. For both ionization methods the molecular ion is observed; however, this high rate of fragmentation for the oxygenated reactant and oxygenated products makes spectral interpretation difficult.

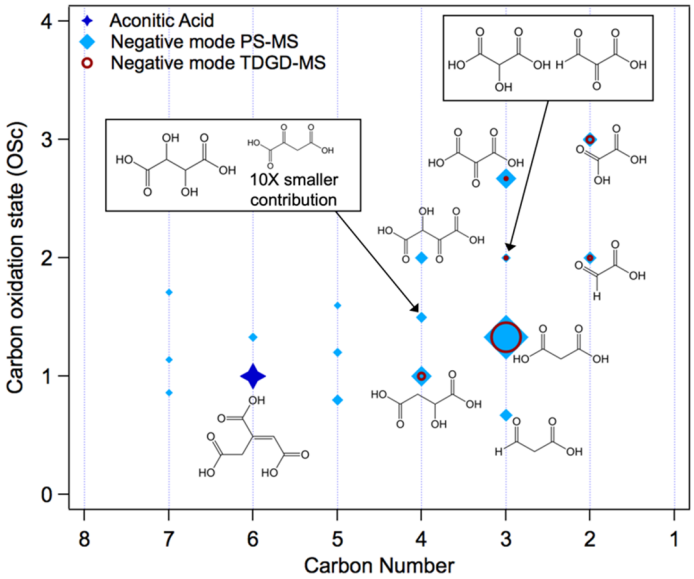

Figure S4: Mean carbon oxidation state (OSc) versus carbon number for major product ions detected by both negative mode paper spray ionization mass spectrometry (PS-MS) and negative mode thermal-desorption glow-discharge ionization mass spectrometry (TDGD-MS). The marker size for product ions correspond to relative intensity in the average mass spectrum of reacted droplets, while the marker size for *trans*-Aconitic Acid is arbitrary. Possible structures, based on exact mass and molecular formulae from high-resolution Orbitrap mass spectra, are shown for C_4 and smaller product ions. We emphasize that these proposed structures do not take into account potential fragmentation pathways during MS detection that likely lead to the same exact masses and molecular formulas, by inference from the fragmentation pathways of *trans*-Aconitic Acid in unreacted droplets. For example, the most intense peak ($C_3H_3O_4^-$) in the TDGD-MS spectra may arise from malonic acid, as suggested in this figure, through a decarboxylation pathway in the particle,[2] or it could arise from sequential loss of CO_2 and H_2O from the C_4 hydroxy hydroperoxide ($C_4H_6O_7$) during detection by either ionization method. We expect the C_4 hydroxy hydroperoxide ($C_4H_6O_7$) is the major product of reaction of the C_4 Criegee Intermediate with water in the aqueous particle.

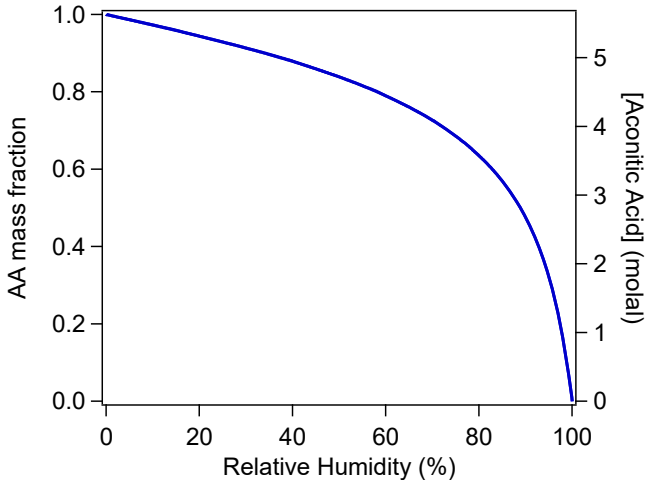

Figure S5: Composition of *trans*-Aconitic Acid ("AA") particles as a function of ambient relative humidity, predicted by the AIOMFAC aerosol thermodynamic model.[3]

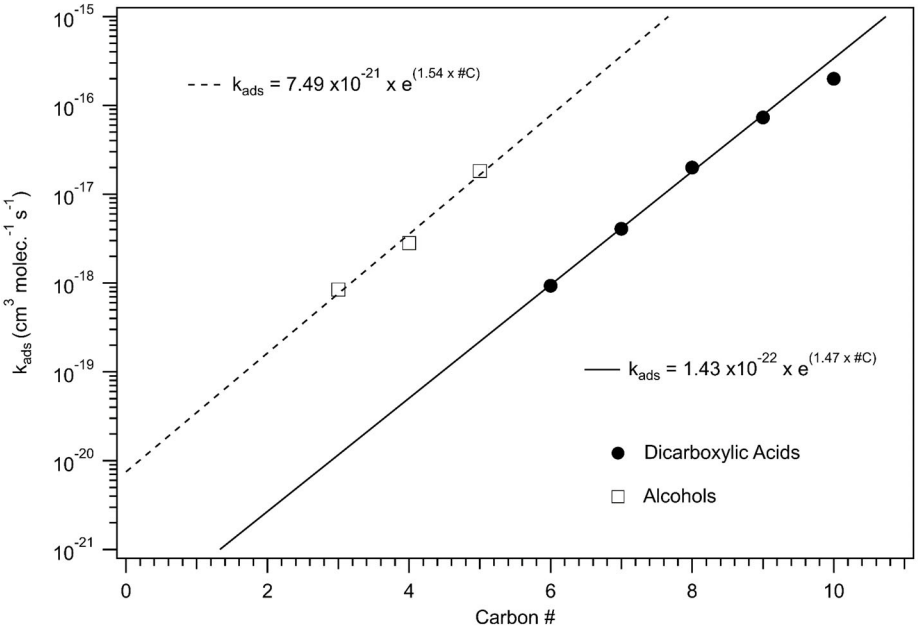

Figure S6. Adsorption rate coefficient (k_{ads}) vs. carbon # for a series of alcohols and dicarboxylic acids from Bleys and Joos.[4] It appears that the C_6 (adipic acid) and C_7 (pimelic acid) values were inadvertently transposed in Table 1 of the original publication, which has been corrected in this figure. Lines are fits to the data that allow extrapolation of k_{ads} to smaller carbon numbers.

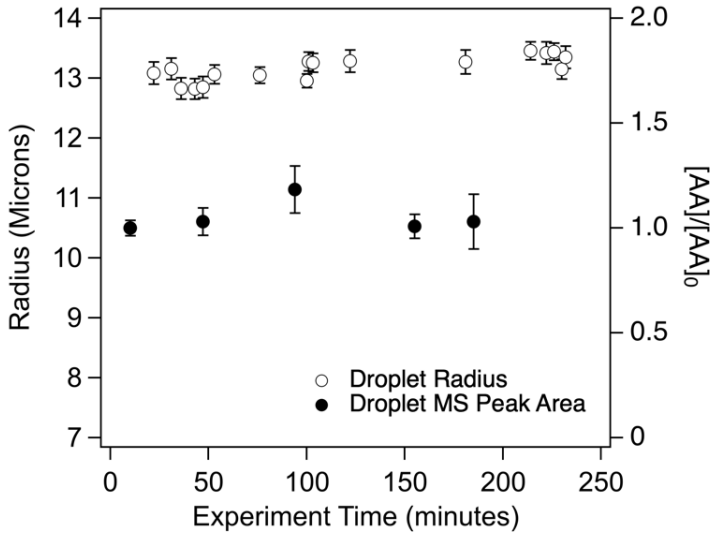

Figure S7: Evaporation control experiment for *trans*-Aconitic Acid ("AA") particles held in the QET for up to ~250 minutes at high relative humidity (89% RH), showing measurements of droplet radius (left axis, open circles) and normalized mean peak area for repeated ejections of single AA droplets from the QET to the thermal-desorption glow-discharge ionization source (right axis, filled circles).

Table S1. Densities, molecular formulas, molecular weight and evaporation rates for species used in the kinetic simulations.

Species	Density (g/mL)	Formula	MW	Evaporation Rate	Vapor Pressure
Aconitic Acid (AA)	1.66	C6H6O6	174		
C4_CI	1.48	C4H4O6	148.07		
Glyoxylic Acid	1.34	C2H2O3	74.03	1.0×10^5 s^{-1}	25 Pa
C3_Product	1.39	C3H4O4	104.06		
C4_Product	1.44	C4H4O5	132.07		
C6_SOZ	1.6	C6H6O9	222.1		
Maleic Acid (MA)	1.4	C4H4O4	116.07	0.07 s^{-1}	see text
C2_CI	1.34	C2H2O4	60.03		
Glyoxylic Acid	1.34	C2H2O3	74.03	1.0×10^5 s^{-1}	25 Pa
C2_Product	1.34	C2H3O5	107.04		
C4_SOZ	1.51	C4H4O7	164.06		

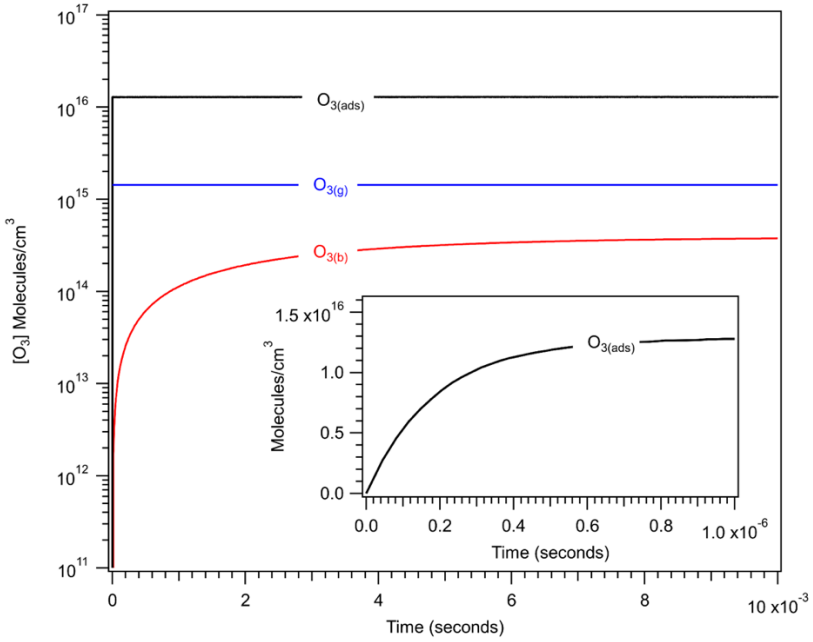

Figure S8: Simulated non-reactive uptake of O_3 to water droplet vs. time showing the partitioning of $O_{3(g)}$ to surface and the bulk. Also shown are the timescales for bulk and surface (see inset) partitioning. Simulations are conducted with a steady state concentration of $O_{3(g)}$. The differences in $[O_{3(g)}]$, $[O_{3(ads)}]$ and $[O_{3(b)}]$ are consistent with H_{cc}^{gs}, H_{cc}^{sb}, and H_{cc}^{gb}. It is interesting to note that the timescale for the bulk ozone to reach steady state is ~5-8 ms, while the interface $[O_{3(ads)}]$ equilibrates 10^4 times faster (i.e. ~500-800 ns). We also note that even for experimental $[O_{3(g)}]$ up to ~ 80 ppm_v, the model does not predict saturation of surface sites with ozone (i.e., $[O_{3(ads)}] < \Gamma_\infty = 5.4 \times 10^{21}$ molecules cm^{-3} given that ozone molecules occupy an area of 18.5 $Å^2$, as computed by Vieceli et al.[5]).

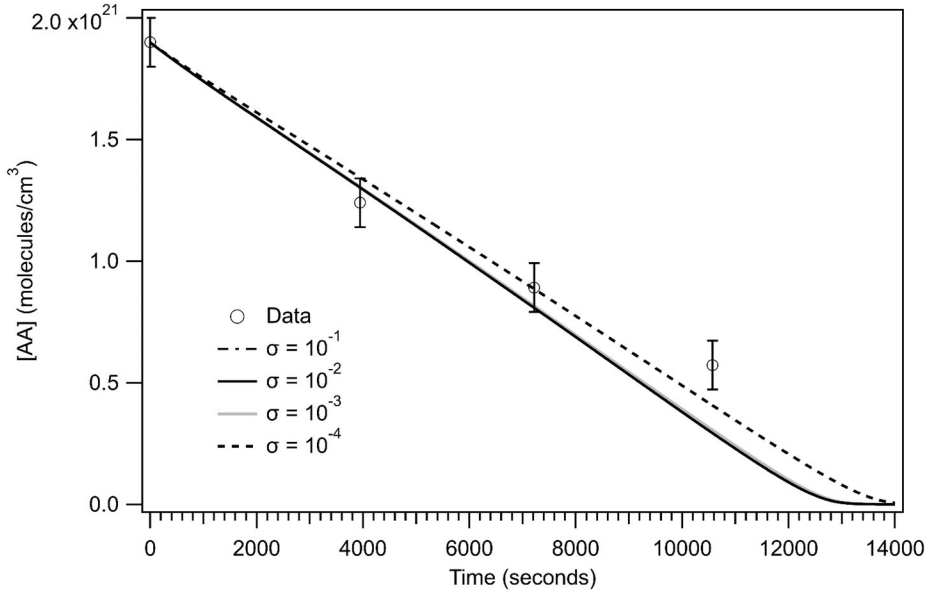

Figure S9. Simulated decay of [AA] vs. time for different value of the sticking coefficient σ. These simulations are run by first changing σ and then adjusting k_{ads}, k_{des}, k_{sol} *and* k_{desolv} to satisfy Eqs. (5) and (7) as described and shown in the main text.

Table S2 List of elementary diffusion and reaction steps with rate coefficients for the surface and bulk regions of the simulation for maleic acid.

	Elementary Step	Rate Coefficient				
No.	***Surface***	**Forward**	**units**	**Reverse**	**Units**	**Ref.**
S1	$O_{3(g)} + O_3\_Site \leftrightarrow O_{3(ads)}$	$(9.0 \times 10^{-11}) \cdot \sigma$	$cm^3\ molec.^{-1}\ s^{-1}$	5.4×10^6	s^{-1}	a,b,c,d
S2	$O_{3(ads)} \leftrightarrow O_{3(b)} + O_3\_Site$	4.6×10^5	s^{-1}	2.8×10^{-15}	$cm^3\ molec.^{-1}\ s^{-1}$	a,b,c,d
S3	$MA_{(ads)} + O_{3(ads)} \rightarrow C_2\_CI_{(ads)} + Glyoxylic\ Acid_{(ads)}$	2.3×10^{-18}	$cm^3\ molec.^{-1} s^{-1}$			e
S4	$C_2\_CI_{(ads)} \rightarrow C_2\_Product_{(ads)}$	7×10^7	s^{-1}			f
S5	$C_2\_CI_{(ads)} + Glyoxylic\ Acid_{(ads)} \rightarrow C_4\_SOZ_{(ads)}$	1.3×10^{-18}	$cm^3\ molec.^{-1} s^{-1}$			f
S6	$C_2\_CI_{(ads)} + O_{3(ads)} \rightarrow Glyoxylic\ Acid_{(ads)}$	4.0×10^{-13}	$cm^3\ molec.^{-1} s^{-1}$			f
S7	$MA_{(b)} + Site \leftrightarrow MA_{(ads)}$	5.07×10^{-20}	$cm^3\ molec.^{-1} s^{-1}$	90	s^{-1}	g
S8	$C_2\_CI_{(b)} + Site \leftrightarrow C_2\_CI_{(ads)}$	2.7×10^{-21}	$cm^3\ molec.^{-1} s^{-1}$	90	s^{-1}	g
S9	$Glyoxylic\ Acid_{(b)} + Site \leftrightarrow Glyoxylic\ Acid_{(ads)}$	2.7×10^{-21}	$cm^3\ molec.^{-1} s^{-1}$	90	s^{-1}	g
S10	$C_2\_Product_{(b)} + Site \leftrightarrow C_2\_Product_{(ads)}$	2.7×10^{-20}	$cm^3\ molec.^{-1} s^{-1}$	90	s^{-1}	g
S11	$C_4\_SOZ_{(b)} + Site \leftrightarrow C_4\_SOZ_{(ads)}$	5.07×10^{-20}	$cm^3\ molec.^{-1} s^{-1}$	90	s^{-1}	g
S12	$MA_{(ads)} \leftrightarrow MA_{(g)} + Site$	0.07	s^{-1}			h
S13	$Glyoxylic\ Acid_{(ads)} \rightarrow Glyoxylic\ Acid_{(g)} + Site$	1.0×10^5	s^{-1}			i
	Diffusion Pathways	**Diffusion Coefficient**				
D1	$MA_{(b)}$ (Bulk) $\leftrightarrow MA_{(b)}$ (Surface)	1.03×10^{-5}	$cm^2\ s^{-1}$			j
D2	$C_2\_CI_{(b)}$ (Bulk) $\leftrightarrow C_2\_CI_{(b)}$ (Surface)	1.2×10^{-5}	$cm^2\ s^{-1}$			j
D3	$Glyoxylic\ Acid_{(b)}$ (Bulk) $\leftrightarrow Glyoxylic\ Acid_{(b)}$ (Surface)	1.2×10^{-5}	$cm^2\ s^{-1}$			j
D4	$C_2\_Product_{(b)}$ (Bulk) $\leftrightarrow C_2\_Product_{(b)}$ (Surface)	1.17×10^{-5}	$cm^2\ s^{-1}$			j
D5	$C_4\_SOZ_{(b)}$ (Bulk) $\leftrightarrow C_4\_SOZ_{(b)}$ (Surface)	8.3×10^{-6}	$cm^2\ s^{-1}$			j
D6	$O_{3(b)}$ (Bulk) $\leftrightarrow O_{3(b)}$ (Surface)	1.76×10^{-5}	$cm^2\ s^{-1}$			k
	Bulk	**Rate Coefficient**				
B1	$MA_{(b)} + O_{3(b)} \rightarrow C_2\_CI_{(b)} + Glyoxylic\ Acid_{(b)}$	2.3×10^{-18}	$cm^3\ molec.^{-1} s^{-1}$			e
B2	$C_2\_CI_{(b)} \rightarrow C_2\_Product_{(b)}$	7.9×10^7	s^{-1}			f
B3	$C_2\_CI_{(b)} + Glyoxylic\ Acid_{(b)} \rightarrow C_4\_SOZ_{(b)}$	1.3×10^{-18}	$cm^3\ molec.^{-1} s^{-1}$			f
B4	$C_2\_CI_{(b)} + O_{3(b)} \rightarrow C_2\_Product_{(b)}$	4.0×10^{-13}	$cm^3\ molec.^{-1} s^{-1}$			f

a: Vacha et al.[6]; **b**: Vieceli et al.[5]; **c**: Sander[7]; **d**: Utter et al.[8], Hu et al.[9], Magi et al.[10], Schütze et al.[11], Müller & Heal[12]; **e**: Leitzke & von Sonntag, **f**: Vereecken et al.[13]; **g**: Bleys and Joos[4]; **h**: Dennis-Smither et al.[14]; **i**: Wiegel et al.[15] ; **j**: Bidstrup and Geankoplis[16]; **k**: Gottschalk et al.[17]; σ is the sticking coefficient.

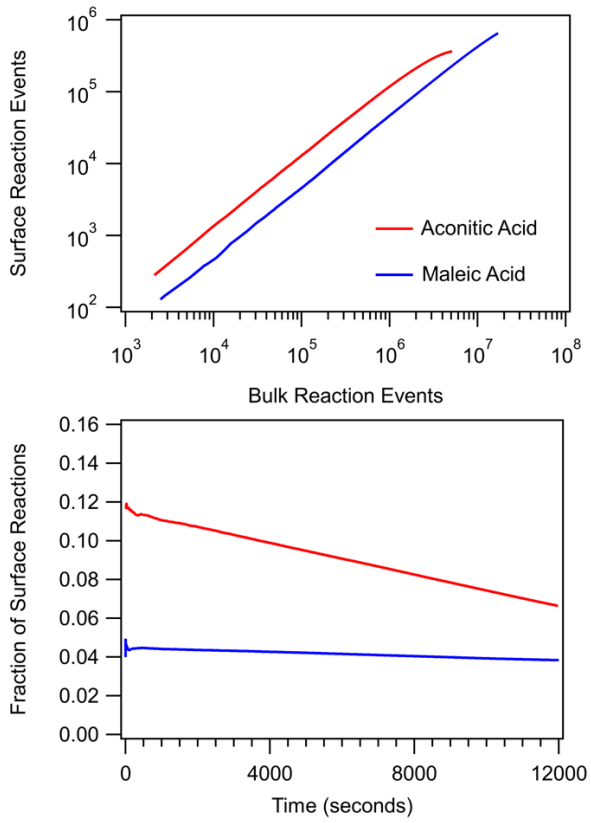

Figure S10: (top) Cumulative surface versus bulk reaction events from explicit simulations for *trans*-Aconitic Acid (red) and Maleic Acid (blue). (bottom) Fraction of surface reaction events as a function of reaction time.

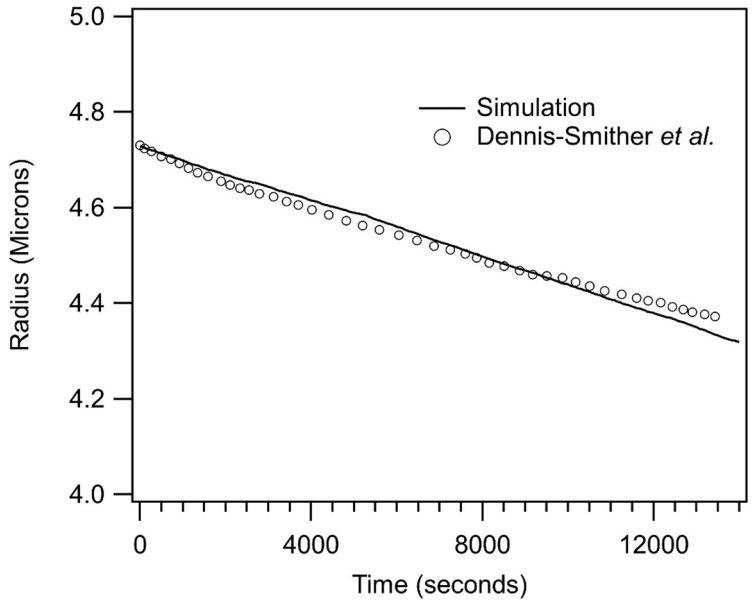

Figure S11. Simulated and measured evaporative change in aqueous maleic droplet size vs. time (without O_3). Data reproduced from Dennis-Smither et al.[14] The MA evaporation rate coefficient, in Table S2 step S12, in the simulation is adjusted to fit the data. This is required since computing the evaporation rate coefficient from the vapor pressure of MA neglects gas phase diffusion limitations that are present in the experiment but not explicitly accounted for in the simulation.

Table S3: Elementary steps, rate and diffusion coefficients used to simulate the oxidation of nitrite by ozone.

	Elementary Step	**Rate Coefficient**				
No.	***Surface***	**Forward**	**units**	**Reverse**	**Units**	**Ref.**
S1	$O_{3(g)} + O_3\_Site \leftrightarrow O_{3(ads)}$	$(9.0 \times 10^{-11}) \cdot \sigma$	$cm^3\ molec.^{-1}\ s^{-1}$	5.4×10^6	s^{-1}	a,b,c,d
S2	$O_{3(ads)} \leftrightarrow O_{3(b)} + O_3\_Site$	4.6×10^5	s^{-1}	2.8×10^{-15}	$cm^3\ molec.^{-1}\ s^{-1}$	a,b,c,d
S3	$Nitrite_{(ads)} + O_{3(ads)} \rightarrow Nitrate_{(ads)} + O_3\_Site$	5.6×10^{-16}	$cm^3\ molec.^{-1} s^{-1}$			e
S4	$Nitrite_{(b)} + Site \leftrightarrow Nitrite_{(ads)}$	5×10^{-19}	$cm^3\ molec.^{-1} s^{-1}$	100	s^{-1}	f
S5	$Nitrate_{(b)} + Nitrate\_Site \leftrightarrow Nitrate_{(ads)}$	3.3×10^{-20}	$cm^3\ molec.^{-1} s^{-1}$	100	s^{-1}	f
	Diffusion Pathways	**Diffusion Coefficient**				
D1	$Nitrite_{(b)}$ (Bulk) $\leftrightarrow Nitrite_{(b)}$ (Surface)	1.42×10^{-5}	$cm^2\ s^{-1}$			g
D2	$Nitrate_{(b)}$ (Bulk) $\leftrightarrow Nitrate_{(b)}$ (Surface)	1.42×10^{-5}	$cm^2\ s^{-1}$			g
D3	$O_{3(b)}$ (Bulk) $\leftrightarrow O_{3(b)}$ (Surface)	1.76×10^{-5}	$cm^2\ s^{-1}$			h
	Bulk	**Rate Coefficient**				
B1	$Nitrite_{(b)} + O_{3(b)} \rightarrow Nitrate_{(b)}$	5.6×10^{-16}	$cm^3\ molec.^{-1} s^{-1}$			e

a: Vacha et al.[6]; **b**: Vieceli et al.[5]; **c**: Sander[7]; **d**: Utter et al.[8], Hu et al.[9], Magi et al.[10], Schütze et al.[11], Müller & Heal[12]; **e**: Garland et al.[18], Hoigne et al.[19]; **f**: Brown et al.[20], Otten et al.[21], Wren & Donaldson[22]; **g**: Yeh et al.[23]; **h**: Gottschalk et al.[17]; σ is the sticking coefficient.

Table S4: Experimental conditions used by Hunt et al. to measure the heterogeneous ozonolysis of nitrite

Droplet #	$[NO_2^-]$ (M)	O_3 (ppm_v)	Diameter (microns)
0	0.2	12	11.5
1	0.36	30.9	11.5
2	0.36	30.9	6.6
3	0.36	30.9	10.4
4	0.36	30.9	9.8
5	0.36	30.9	12
6	0.2	6.76	9.3
7	0.2	6.76	8.6
8	0.2	6.76	10.7
9	0.2	6.76	10.3

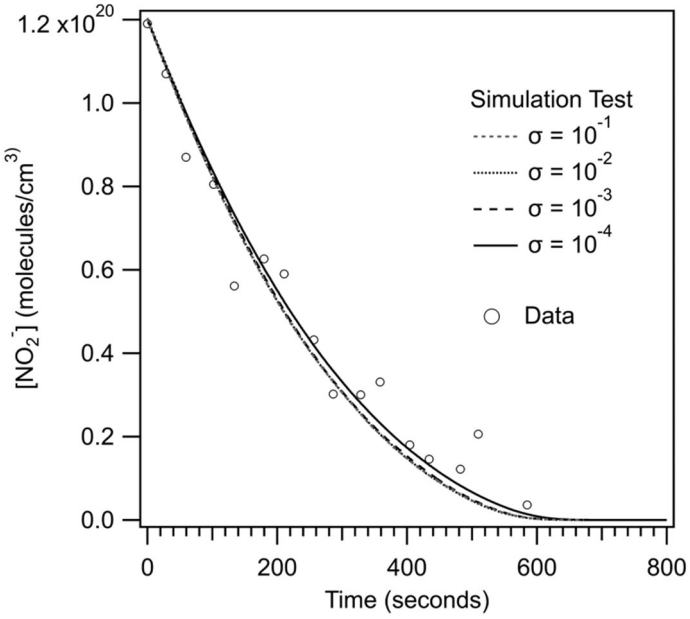

Figure S12: Sensitivity of sodium nitrite simulations to the assumed value of the sticking coefficient for ozone on the surface of aqueous particles. Experimental data is from Hunt et al.[24]

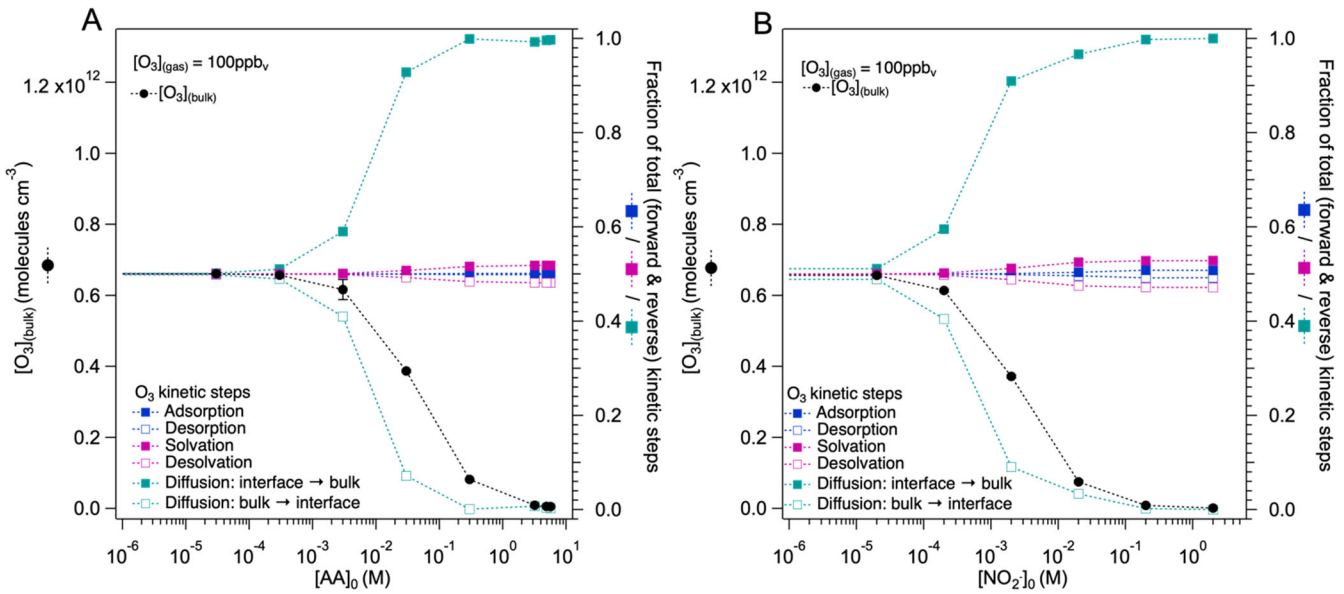

Figure S13: Bulk O_3 concentrations and fractional frequencies of forward and reverse O_3 kinetic steps (i.e., adsorption/desorption, solvation/desolvation and interface ↔ bulk diffusion), from stochastic kinetic simulations for *trans*-Aconitic Acid (A) and Sodium Nitrite (B), corresponding to simulation data shown in Figure 9 of the main text. Frequencies are shown as a fraction of total forward and reverse kinetic "events" simulated by the Kinetiscope model. These frequencies can be interpreted as the relative importance of a specific kinetic step in the model, and over a constant simulation time period could be interpreted as an overall rate. Increasing solute concentrations perturb the coupled gas-interface and interface-bulk coupled kinetic steps such that desolvation, desorption and bulk to interface diffusion frequencies decrease, while adsorption, solvation and interface to bulk diffusion frequencies increase. As solute concentration increases in our simulations the adsorbed ozone concentration is constant (Figure 8, main text), but the bulk ozone concentration increasingly deviates from its Henry's Law value. This arises from limitations in the rate of interface to bulk diffusion, which contributes 100% of diffusion events at high solute concentrations.

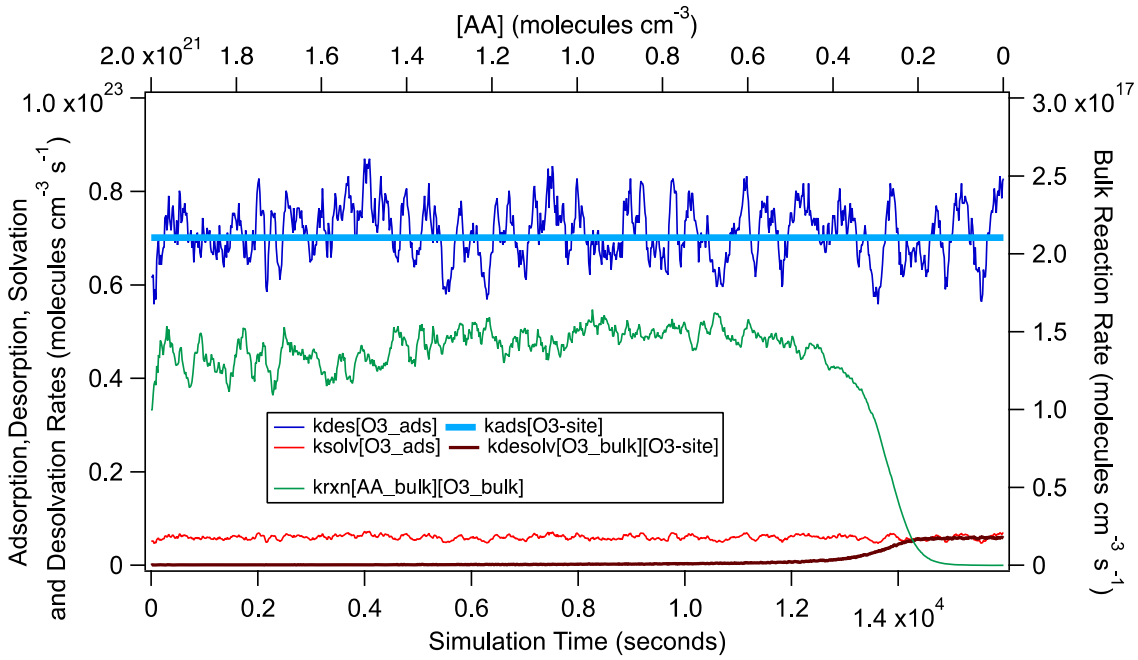

Figure S14: (left axis) Rates of O_3 adsorption and desorption (blue lines), solvation and desolvation (red lines), and (right axis) the rate of bulk reaction (green line), over the reaction timescale for an AA particle under conditions corresponding to Expt #1 (main text, Table 1). The bulk reaction rate is 4 orders of magnitude slower than the solvation and desolvation rates, and 6 orders of magnitude slower than the adsorption and desorption rates. The noise in desorption, solvation and reaction rates corresponds to stochastic variability, and have been smoothed with a 10-point running average. The adsorption rate is fixed, because we fix the gas phase O_3 concentration in our simulation at the experimentally measured value and conserve the number of available O_3 adsorption sites.

References

1. Willis, M. D.; Rovelli, G.; Wilson, K. R., Combining mass spectrometry of picoliter samples with a multi-compartment electrodynamic trap for probing the chemistry of droplet arrays. *Anal Chem* **2020**.
2. Leitzke, A.; Sonntag, C. v., Ozonolysis of Unsaturated Acids in Aqueous Solution: Acrylic, Methacrylic, Maleic, Fumaric and Muconic Acids. *Ozone: Science & Engineering* **2009,** *31* (4), 301-308.
3. Zuend, A.; Marcolli, C.; Booth, A. M.; Lienhard, D. M.; Soonsin, V.; Krieger, U. K.; Topping, D. O.; McFiggans, G.; Peter, T.; Seinfeld, J. H., New and extended parameterization of the thermodynamic model AIOMFAC: calculation of activity coefficients for organic-inorganic mixtures containing carboxyl, hydroxyl, carbonyl, ether, ester, alkenyl, alkyl, and aromatic functional groups. *Atmos. Chem. Phys.* **2011,** *11* (17), 9155-9206.
4. Bleys, G.; Joos, P., Adsorption kinetics of bolaform surfactants at the air/water interface. *The Journal of Physical Chemistry* **1985,** *89* (6), 1027-1032.
5. Vieceli, J.; Roeselova, M.; Potter, N.; Dang, L. X.; Garrett, B. C.; Tobias, D. J., Molecular Dynamics Simulations of Atmospheric Oxidants at the Air-Water Interface: Solvation and Accommodation of OH and O3. *J Phys Chem B* **2005,** *109*, 15876-15892.
6. Vacha, R.; Slavicek, P.; Mucha, M.; Finlayson-Pitts, B. J.; Jungwirth, P., Adsorption of Atmospherically Relevant Gases at the Air/Water Interface: Free Energy Profiles of Aqueous Solvation of N2, O2, O3, OH, H2O, HO2, and H2O2. *J Phys Chem A* **2004,** *108*, 11573-11579.
7. Sander, R., Compilation of Henry's law constants (version 4.0) for water as solvent. *Atmospheric Chemistry and Physics* **2015,** *15* (8), 4399-4981.
8. Utter, R. G.; Burkholder, J. B.; Howard, C. J.; Ravishankara, A. R., Measurement of the mass accommodation coefficient of ozone on aqueous surfaces. *The Journal of Physical Chemistry* **1992,** *96* (12), 4973-4979.
9. Hu, J. H.; Shi, Q.; Davidovits, P.; Worsnop, D. R.; Zahniser, M. S.; Kolb, C. E., Reactive Uptake of Cl2(g) and Br2(g) by Aqueous Surfaces as a Function of Br- and I- Ion Concentration: The Effect of Chemical Reaction at the Interface. *The Journal of Physical Chemistry* **1995,** *99* (21), 8768-8776.
10. Magi, L.; Schweitzer, F.; Pallares, C.; Cherif, S.; Mirabel, P.; George, C., Investigation of the Uptake Rate of Ozone and Methyl Hydroperoxide by Water Surfaces. *The Journal of Physical Chemistry A* **1997,** *101* (27), 4943-4949.
11. Schütze, M.; Herrmann, H., Determination of phase transfer parameters for the uptake of HNO3, N2O5 and O3 on single aqueous drops. *Physical Chemistry Chemical Physics* **2002,** *4* (1), 60-67.
12. Müller, B.; Heal, M. R., The mass accommodation coefficient of ozone on an aqueous surface. *Physical Chemistry Chemical Physics* **2002,** *4* (14), 3365-3369.
13. Vereecken, L.; Harder, H.; Novelli, A., The reactions of Criegee intermediates with alkenes, ozone, and carbonyl oxides. *Phys Chem Chem Phys* **2014,** *16* (9), 4039-49.
14. Dennis-Smither, B. J.; Marshall, F. H.; Miles, R. E.; Preston, T. C.; Reid, J. P., Volatility and oxidative aging of aqueous maleic acid aerosol droplets and the dependence on relative humidity. *J Phys Chem A* **2014,** *118* (30), 5680-91.
15. Wiegel, A. A.; Wilson, K. R.; Hinsberg, W. D.; Houle, F. A., Stochastic methods for aerosol chemistry: a compact molecular description of functionalization and fragmentation in the heterogeneous oxidation of squalane aerosol by OH radicals. *Physical Chemistry Chemical Physics* **2015,** *17* (6), 4398-4411.
16. Bidstrup, D. E.; Geankoplis, C. J., Aqueous Molecular Diffusivities of Carboxylic Acids. *Journal of Chemical & Engineering Data* **1963,** *8* (2), 170-173.
17. Gottschalk, C.; Libra, J. A.; Saupe, A., *Ozonation of Water and Waste Water: A Practical Guide to Understanding Ozone and its Applications*. 2 ed.; Wiley-VCH Verlag GmbH & Co.: 2010.
18. Garland, J. A.; Elzerman, A. W.; Penkett, S. A., The mechanism for dry deposition of ozone to seawater surfaces. *Journal of Geophysical Research: Oceans* **1980,** *85* (C12), 7488-7492.

19. Hoigné, J.; Bader, H.; Haag, W. R.; Staehelin, J., Rate constants of reactions of ozone with organic and inorganic compounds in water—III. Inorganic compounds and radicals. *Water Research* **1985,** *19* (8), 993-1004.
20. Brown, M. A.; Winter, B.; Faubel, M.; Hemminger, J. C., Spatial Distribution of Nitrate and Nitrite Anions at the Liquid/Vapor Interface of Aqueous Solutions. *Journal of the American Chemical Society* **2009,** *131* (24), 8354-8355.
21. Otten, D. E.; Onorato, R.; Michaels, R.; Goodknight, J.; Saykally, R. J., Strong surface adsorption of aqueous sodium nitrite as an ion pair. *Chemical Physics Letters* **2012,** *519-520*, 45-48.
22. Wren, S. N.; Donaldson, D. J., Glancing-angle Raman study of nitrate and nitric acid at the air–aqueous interface. *Chemical Physics Letters* **2012,** *522*, 1-10.
23. Yeh, H. S.; Wills, G. B., Diffusion coefficient of sodium nitrate in aqueous solution at 25.deg. as a function of concentration from 0.1 to 1.0M. *Journal of Chemical & Engineering Data* **1970,** *15* (1), 187-189.
24. Hunt, O. R.; Ward, A. D.; King, M. D., Heterogeneous oxidation of nitrite anion by gas-phase ozone in an aqueous droplet levitated by laser tweezers (optical trap): is there any evidence for enhanced surface reaction? *Physical Chemistry Chemical Physics* **2015,** *17* (4), 2734-2741.